POLITECNICO DI TORINO
Repository ISTITUZIONALE

Experimental ride comfort assessment of electric kick scooters under urban driving scenarios

Original
Experimental ride comfort assessment of electric kick scooters under urban driving scenarios / Vella, A.D., Vigliani, A.. - In: VEHICLE SYSTEM DYNAMICS. - ISSN 0042-3114. - (2026), pp. 1-34. [10.1080/00423114.2026.2735368]

Availability:
This version is available at: 11583/3016387 since: 2026-10-07T08:03:04Z

Publisher:
Taylor & Francis Group

Published
DOI:10.1080/00423114.2026.2735368

Terms of use:

This article is made available under terms and conditions as specified in the corresponding bibliographic description in the repository

Publisher copyright

(Article begins on next page)

12 November 2026

Taylor & Francis
Taylor & Francis Group

Vehicle System Dynamics
International Journal of Vehicle Mechanics and Mobility

ISSN: 0042-3114 (Print) 1744-5159 (Online) Journal homepage: www.tandfonline.com/journals/nvsd20

Experimental ride comfort assessment of electric kick scooters under urban driving scenarios

Angelo Domenico Vella & Alessandro Vigliani

To cite this article: Angelo Domenico Vella & Alessandro Vigliani (06 Oct 2026): Experimental ride comfort assessment of electric kick scooters under urban driving scenarios, Vehicle System Dynamics, DOI: 10.1080/00423114.2026.2735368

To link to this article: https://doi.org/10.1080/00423114.2026.2735368

© 2026 The Author(s). Published by Informa UK Limited, trading as Taylor & Francis Group.

Published online: 06 Oct 2026.

Submit your article to this journal

View related articles

View Crossmark data

Full Terms & Conditions of access and use can be found at
https://www.tandfonline.com/action/journalInformation?journalCode=nvsd20

VEHICLE SYSTEM DYNAMICS
https://doi.org/10.1080/00423114.2026.2735368

OPEN ACCESS Check for updates

Experimental ride comfort assessment of electric kick scooters under urban driving scenarios

Angelo Domenico Vella and Alessandro Vigliani

Department of Mechanical and Aerospace Engineering, Politecnico di Torino, Torino, Italy

ABSTRACT

Ride comfort represents a critical yet still under-investigated aspect in the design of electric kick scooters, despite their widespread use in urban mobility. This work presents an experimental assessment of vibration-induced discomfort under real riding conditions. Three vehicles with different layouts are tested at constant speeds on representative road surfaces. Dedicated laboratory tests are carried out to characterise vehicle mass properties and tyre radial stiffness and to support the interpretation of on-road vibration measurements. Accelerations transmitted to the rider at the foot-deck and hand-steering interfaces are recorded and processed according to ISO standards for whole-body and hand-transmitted vibrations, enabling an objective and quantitative comparison among vehicles. The results highlight a significant degradation of ride comfort on irregular surfaces and a strong dependence of discomfort levels on vehicle speed. A regression analysis is conducted to relate the measured discomfort indices to key vehicle characteristics and operating parameters. Vehicle speed emerges as the dominant factor influencing the vibration response, while road surface roughness and tyre radial stiffness provide secondary but significant contributions. The proposed regression model captures the main experimental trends across different vehicles, speeds and surfaces, and supports a quantitative understanding of the mechanisms governing ride comfort in electric kick scooters.

ARTICLE HISTORY
Received 25 February 2026
Revised 16 July 2026
Accepted 13 September 2026

KEYWORDS
Electric kick scooter; urban mobility; ride comfort; whole-body vibrations; hand-transmitted vibrations; regression model

List of symbols

a_{ij}	Raw acceleration at the human–vehicle interface i along direction j
$\bar{a}_{ij}$	ISO-filtered acceleration at the human–vehicle interface i along direction j
a_{ij}^{RMS}	Root mean square of the ISO-filtered acceleration at the human–vehicle interface i along direction j
a_{ij}^{Max}	Maximum absolute value of the ISO-filtered acceleration at the human–vehicle interface i along direction j
c	Vehicle and surface case
CF_{ij}	Crest factor at the human–vehicle interface i along direction j
d	Steering column length

CONTACT Angelo Domenico Vella angelo.vella@polito.it

© 2026 The Author(s). Published by Informa UK Limited, trading as Taylor & Francis Group.
This is an Open Access article distributed under the terms of the Creative Commons Attribution License (http://creativecommons.org/licenses/by/4.0/), which permits unrestricted use, distribution, and reproduction in any medium, provided the original work is properly cited. The terms on which this article has been published allow the posting of the Accepted Manuscript in a repository by the author(s) or with their consent.

D	Foot-deck measuring point
DI_i	Discomfort index at the human–vehicle interface i
e	Experimental observation index
E	Total number of experimental observations
F	Front wheel hub point
$f_{1,\ldots,10}$	Frequencies used in the computation of H_{ij}
G	Vehicle centre of gravity
h	Centre of mass distance along $\boldsymbol{z}$ from F
$H_{b,j}$	Band-pass filter prescribed by ISO 5349 along direction j
$H_{h,j}$	High-pass filter prescribed by ISO 2631-1 along direction j
$H_{l,j}$	Low-pass filter prescribed by ISO 2631-1 along direction j
$H_{t,j}$	First frequency filter prescribed by ISO 2631-1 along direction j
$H_{s,j}$	Second frequency filter prescribed by ISO 2631-1 along direction j
$H_{w,j}$	Frequency filter prescribed by ISO 5349 along direction j
H_{ij}	ISO weighting transfer function at the human–vehicle interface i along direction j
$\mathcal{H}_{ij}$	Time-domain ISO weighting operator at the human–vehicle interface i along direction j
i	Interface index (D, S)
j	Vibration direction index ($\boldsymbol{x}$, $\boldsymbol{y}$, $\boldsymbol{z}$)
k_{ij}	Directional multiplying factors at the human–vehicle interface i along direction j for the computation of the discomfort index
l	Centre of mass distance along $\boldsymbol{x}$ from F
m	Vehicle mass
L_z	Applied vertical load during the tyre characterisation
n_c	Number of observations associated with vehicle-surface case c
n_r	Number of regressors in the regression model
$N_{F/R}$	Front and rear vertical wheel reaction force under steady-state conditions
$P_{1/2}$	Suspension points during the suspension tests
q_R	Road surface coefficient
$Q_{1,\ldots,10}$	Coefficients used in the computation of the ISO weighting filters H_{ij}
p	Variable of the Laplace transform
p_a	Nominal tyre inflation pressure
r	Unloaded tyre radius
R^2	Coefficient of determination
S	Hand-steering measuring point
$\mathrm{S}_{1/2/3}$	Road surface
t	Time variable
T	Duration of the segment used in the signal processing
$\boldsymbol{u}_e$	Regressor vector associated with observation e
v	Vehicle speed
$\mathrm{V}_{1/2/3}$	Vehicle
w	Vehicle wheelbase
w_e	Weighting factor used to equalise the contribution in the regression
$\boldsymbol{x}$	Longitudinal axis of the vehicle reference frame
$\boldsymbol{y}$	Lateral axis of the vehicle reference frame

$\boldsymbol{z}$	Vertical axis of the vehicle reference frame
$\boldsymbol{\alpha}_i$	Regression coefficient vector at the human–vehicle interface i
$\beta_{1/2}$	Inclination of the suspension lines w. r. t. $\boldsymbol{z}$ and $\boldsymbol{x}$
δ	Tyre radial deflection during the tyre characterisation
γ	Inclination of the steering column with respect to $\boldsymbol{z}$
$\kappa_{F/R}$	Front and rear tyre radial stiffness under steady-state operating load
κ_0	Average operational tyre radial stiffness
μ	Mean crest factor
σ	Standard deviation of the crest factor
$\omega_{1,\ldots,10}$	Angular frequencies used in the computation of H_{ij}

1. Introduction

Ride comfort represents a key performance attribute in the design and assessment of wheeled vehicles, as it directly influences user acceptance, perceived quality, and indirectly safety during operation [1]. Mechanical vibrations generated by the interaction between the vehicle and road surfaces are transmitted to the human body through multiple contact interfaces, producing sensations that range from mild to severe annoyance and, in some cases, adverse effects on well-being [2]. For these reasons, the quantitative evaluation of vibration-induced discomfort has long been a central topic in vehicle dynamics, ergonomics, and human–machine interaction research [3–5].

Over the past decades, ride comfort has been extensively investigated in a wide range of transportation systems, including road vehicles such as passenger cars, buses, and trucks [6–8], rail vehicles [9–11], and aircraft [12–14]. In this context, ride comfort assessment has increasingly relied on objective and standardised methodologies grounded in experimental vibration analysis and human response modelling, while subjective evaluations have remained essential for capturing the perceptual dimension of comfort. A consistent outcome of this research is the recognition that human perception of vibrations depends not only on their amplitude, but also on frequency content, direction, exposure duration, and the specific body regions involved in the transmission process [15–17]. Accordingly, an important research stream has focused on relating objective vibration descriptors to subjective comfort and discomfort ratings, using both correlation analyses and regression-based models [18,19]. Such integrated approaches are particularly valuable because objective metrics and subjective ratings capture complementary aspects of the same phenomenon: the former provide repeatable and physically interpretable quantities, whereas the latter reflect user perception and individual sensitivity.

From a biomechanical standpoint, the response of the human body to mechanical vibrations reflects the complex dynamic behaviour of the musculoskeletal system, characterised by frequency-dependent sensitivity and directional anisotropy. Several studies have shown that variations in vibration direction, frequency bands, posture and contact conditions may lead to markedly different discomfort sensations even at comparable acceleration levels, highlighting the importance of appropriate frequency weighting and interface-specific evaluation criteria [20,21]. Accordingly, vibrations transmitted to the human body are commonly classified into whole-body vibrations (WB) and hand-transmitted (HT) vibrations, depending on the dominant contact interfaces and posture of the subject: the former

typically involve transmission through the feet, seat, or back, whereas the latter primarily affect the upper limbs through steering or control interfaces.

To provide a consistent and objective basis for the evaluation of human exposure to mechanical vibrations, international standards have been developed and widely adopted. In particular, ISO 2631-1 [22] defines procedures for the measurement, frequency weighting, and evaluation of WB vibrations under different postures and applications, including comfort assessment, vibration perception, motion sickness, and health-related monitoring. In parallel, ISO 5349-1 [23] establishes analogous methodologies for HT vibrations. These standards, together with the earlier British Standard BS 6841 [24], constitute the consolidated framework for experimental ride comfort assessment in conventional transportation systems and have been extensively applied in both academic research and industrial practice.

While these ISO-based procedures were originally developed for conventional vehicles and working machinery, their direct transfer to emerging vehicle categories with substantially different layouts and rider postures requires careful interpretation and experimental validation. These aspects become particularly relevant when considering lightweight and compact electric micro-vehicles (e-MVs), where the coupling between the rider and the vehicle is stronger and the vibrational environment may differ markedly from that of traditional vehicles.

In recent years, electric kick scooters (e-scooters) have undergone rapid growth in urban environments, becoming one of the most prominent modes of micromobility. Their success is commonly attributed to their compact dimensions, ease of use, and suitability for short-distance trips, especially in dense urban contexts [25–29]. Several studies have documented how e-scooters have been progressively integrated into urban transport systems, either as complementary modes to public transport or as standalone solutions for short trips, contributing to changes in travel behaviour and modal choice [30–34]. Analyses of usage patterns consistently indicate that e-scooter trips are typically short and often occur in mixed-traffic environments, including bike lanes, sidewalks, and local streets, where pavement quality may vary significantly [35]. From the user perspective, acceptance studies further show that perceived ride quality, physical effort, and overall comfort play a non-negligible role in the adoption and continued use of shared e-scooter services, especially for repeated or daily trips [36,37]. The relevance of e-scooters within urban mobility systems has been further amplified during the COVID-19 pandemic, which significantly altered travel demand and mode preferences. Several contributions report that micromobility services, including shared e-scooters, gained importance during periods of mobility restrictions, offering flexible and socially distanced alternatives to conventional public transport [38–40]. Within this rapidly evolving scenario, the engineering characterisation of e-scooters has not progressed at the same pace as their urban deployment. While a substantial body of literature addresses policy, safety, and usage aspects, fewer studies focus on the mechanical interaction between e-scooters, road irregularities, and riders, particularly from the perspective of vibration transmission and ride comfort. This gap is especially relevant given the diverse and often suboptimal surface conditions encountered in real urban operation.

Despite apparent similarities with other light two-wheeled vehicles, e-scooters exhibit a set of distinctive dynamic and structural characteristics that make their analysis fundamentally different from that of bicycles and small mopeds [41–43]. One of the most critical

aspects is the adoption of very small wheels, which significantly increases sensitivity to road irregularities and local surface defects, while also affecting stability and controllability [44,45]. From a structural standpoint, most commercial e-scooters are characterised by the absence of suspension systems or, in some cases, by the presence of simplified and poorly tuned suspensions. As a result, vibration attenuation is often limited to the compliance of the tyres, leading to a filtering effect that acts primarily at the wheel level and provides limited isolation of the rider from road-induced excitations. A further distinguishing feature lies in the mass distribution of the vehicle–rider system: in e-scooters, the mass of the rider is always dominant with respect to that of the vehicle, resulting in a strongly rider–driven dynamic behaviour [46]. Finally, the standing riding posture and the absence of a dedicated seating system eliminate a major vibration isolation interface and reduce the human–machine interaction to essentially two contact points, i.e. the foot-deck and hand-steering interfaces.

From an engineering perspective, recent literature on e-scooters has developed along three main directions: rider–vehicle dynamics and handling, vibration/comfort assessment in real operating conditions, and physics-based modelling of longitudinal/vertical response. Experimental studies have investigated the rider behaviour and the vehicle dynamics during typical manoeuvres [47,48], while several contributions have addressed vibration exposure and comfort-related aspects through on-road measurements and comparative analyses [49–53]. In parallel, lumped–parameter and multibody models have been proposed to describe the vertical dynamics of e-scooters under distributed road irregularities and discrete obstacles [54–57]. Overall, these studies confirm the growing maturity of experimental and modelling tools for e-scooters, but they also highlight the need for systematic comfort benchmarks capable of linking measured vibration metrics to vehicle design features and operating conditions. To clarify the positioning of the present contribution within the existing literature, Table 1 summarises selected studies on e-scooter dynamics, vibration exposure and ride comfort, distinguishing them in terms of methodological approach, investigated vehicles, riders, test conditions and research focus.

Against this background, the objective of this work is to provide a quantitative experimental assessment of ride comfort in commercial electric kick scooters under real driving conditions, using an ISO–based framework to interpret the vibrations transmitted to the rider. Differently from recent studies focusing on the vertical response of a single e-scooter under a limited set of discrete operating conditions [58], or on the influence of inter-subject variability when riding the same platform [59], the present work adopts a broader experimental perspective. Three e-scooters characterised by different layouts are tested across their full operational speed range on three representative urban pavement surfaces. Vibrations are measured at the two human–machine interfaces dictated by the standing posture, i.e. foot-deck and hand-steering, and processed according to WB and HT vibration standards. Further laboratory tests are conducted to characterise vehicle mass properties and tyre radial stiffness, enabling a physically grounded link between design parameters, operating conditions and discomfort outcomes. The added value of the proposed approach therefore lies in the integration of three complementary levels of analysis. First, ISO-based WB and HT vibration metrics provide a standardised and interface-specific quantification of the vibrations transmitted to the standing rider. Secondly, laboratory characterisation of mass distribution and tyre radial stiffness allows interpreting the differences among vehicles in terms of measurable physical properties rather than only in terms of nominal vehicle

Table 1. Summary of the studies on e-scooter dynamics classified by methodological approach (experimental and/or numerical), experimental conditions (number of vehicles, surfaces, and speeds), and research focus.

Study	Approach		No. of				Focus
	Exp.	Num.	Vehicles	Surfaces	Speeds	Riders	
Paudel [44]		✓	27 config.	Flat	Parametric, full range	1, 2 postures	Steering design, self-stability
Agundez [45]		✓	1	Flat	Parametric, full range	1	Multibody modelling, linear stability analysis
Garman [47]	✓		1	1 test track, 3 brak. surf.	Manoeuvre-dependent	8	Vehicle dynamics, rider kinematics
Brunner [48]	✓		1	1 test track	15km/h	24	Rider behaviour, stability
Cano-Moreno [49]	✓	✓	1	4 ISO 8608 road classes	5, 10, 15, 20, 25km/h	1	Comfort and health assessment, multibody simulation
Cano-Moreno [50]	✓		1	2, asphalt and pavers	Not constant	N.A.	Health-risk assessment of WB and HT vibrations
Gulino [51]	✓		1 platform, different decks	6 obstacles	Up to 25km/h	1	Effect of deck material on ISO-based comfort
Boglietti [52]	✓		1 e-scooter, 1 e-bike	5 paths: bituminous, uneven and regular cobblestone, metal grids, dirt/concrete	10, 12.5 and 15km/h	6	Comfort comparison between e-scooter/bike
Ventura [53]	✓	✓	1 e-scooter, 1 e-bike		10 and 15km/h		Framework for comparing e-scooter and e-bike vibration comfort using experimental and simulated data
Asperti [54]	✓	✓	1	Lumped obstacles	17 and 19km/h	1	Lumped-parameter vertical dynamics model
Asperti [55]	✓	✓	1	Distributed irregularities	17 and 23km/h	1	
Arslan [56]		✓	1	Curb	6, 8, 10km/h	Parametric	Dynamic response stability
Vaca Michilena [57]		✓	1	2	10/20/30km/h	1	Effect of tyre stiffness on vibration comfort
Asperti [58]	✓	✓	1	4	6, 13, 18/20km/h	4	Vertical dynamics, influence of pavement, speed, tyre pressure and rider mass

categories. Thirdly, the regression framework combines this objective discomfort indicator with vehicle and operating parameters, enabling the effect of speed, surface condition and tyre stiffness to be quantified within a compact and physically interpretable model. This integrated perspective extends previous experimental studies mainly focused on individual vehicles, single road surfaces, or narrower operating ranges, and provides a comparative basis for identifying the main design- and operation-related factors governing e-scooter ride comfort.

The novel contributions of this work are:

- comparative ISO–based vibration benchmarking of three commercial e-scooters with markedly different layouts (e.g. mass distribution, motor/brake arrangements, tyre characteristics, and suspension systems);
- laboratory characterisation of vehicle inertial properties and tyre radial stiffness, used to support the physical interpretation of the differences observed in the on-road comfort measurements;

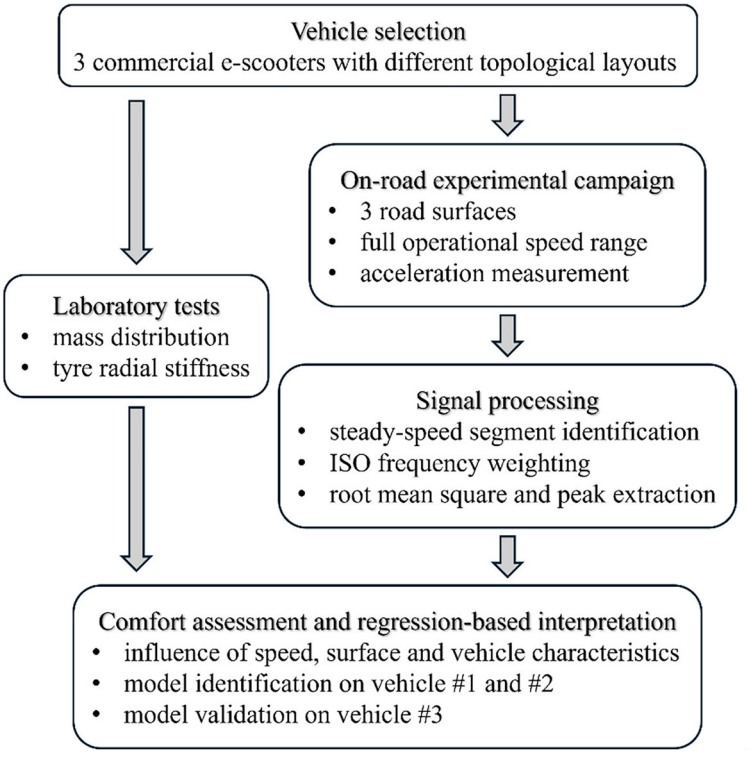

Figure 1. Overview of the proposed framework for e-scooter ride comfort assessment, linking vehicle characterisation, on-road vibration measurements, ISO-based signal processing and regression-based interpretation.

- development of a compact regression model combining ISO-based ride quality indicators with experimentally measured vehicle properties and operating conditions, to assess the role of speed, road surface and tyre radial stiffness in rider discomfort.

The overall workflow of the study is summarised in Figure 1, which illustrates how vehicle selection and laboratory characterisation are combined with on-road vibration measurements, ISO-based signal processing and regression-based interpretation.

The manuscript is organised as follows. Section 2 describes the analysed vehicles and the laboratory tests performed to characterise the vehicle mass distribution and the tyre stiffness. Section 3 presents the on-road campaign, focusing on sensor setup, test protocol, and signal processing. Section 4 discusses the experimental results, the regression-based interpretation, the practical implications and the main limitations of the study, while concluding remarks are drawn in Section 5.

2. Vehicle description and physical characterisation

In this study, three commercial e-scooters are analysed, as shown in Figure 2. Although they target a similar market segment and price range, the selected models differ significantly in terms of vehicle layout and component configuration. These differences are

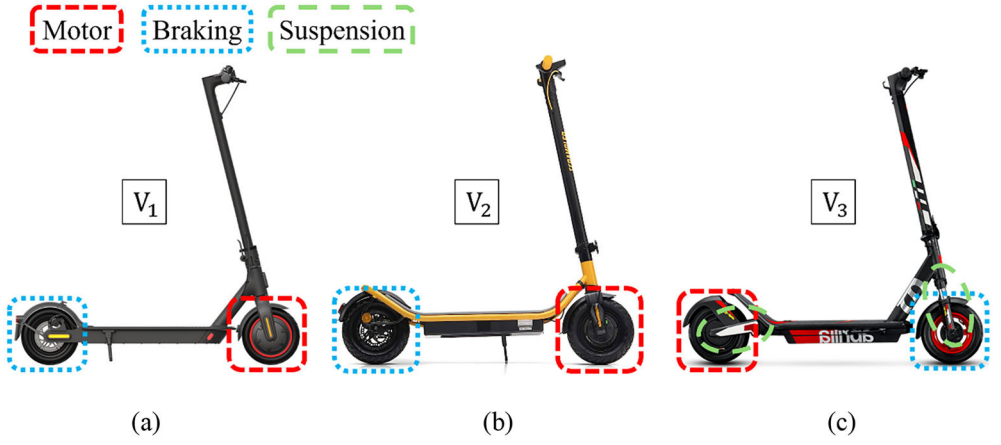

Figure 2. E-scooters analysed in this study with their key layout differences: (a) V_1, (b) V_2, and (c) V_3.

Table 2. Summary of the technical data, mass properties, and wheel vertical loads of the three e-scooters (values in brackets indicate the vertical load with the rider on the vehicle).

		Vehicle		
		V_1	V_2	V_3
Technical data	w [m]	0.875	0.895	0.940
	d [m]	1.065	1.050	1.045
	γ [deg]	14	12	12.5
	r [inch]	8.5	10	11
	p_a [bar]	3.5	2.0	2.5
Centre of mass	m [kg]	14.2	17.3	16.5
	l [m]	0.340	0.455	0.450
	h [m]	0.115	0.115	0.145
Vertical load	N_F [N]	86.4(340.3)	83.4(359.5)	84.4(383.6)
	N_R [N]	54.9(561.2)	86.3(570.5)	77.5(538.5)

expected to influence the transmission and filtering of road-induced vibrations through the e-scooter structure, thereby affecting the vibration levels reaching the rider and the resulting ride comfort.

In the left-hand (V_1) and middle (V_2) vehicles, the electric motor (red dashed outline) is integrated into the front wheel, while the mechanical braking system (blue dotted outline) is located at the rear and consists of a disc brake. In contrast, the right-hand e-scooter (V_3) adopts an opposite configuration, with the motor housed in the rear wheel and a front drum brake. Moreover, V_3 is equipped with a basic suspension system (green dashed outline) at both the front and rear wheels, whereas V_1 and V_2 feature rigid, unsuspended architectures. Other technical differences among the three e-scooters are highlighted in Table 2 in Section 2.1.

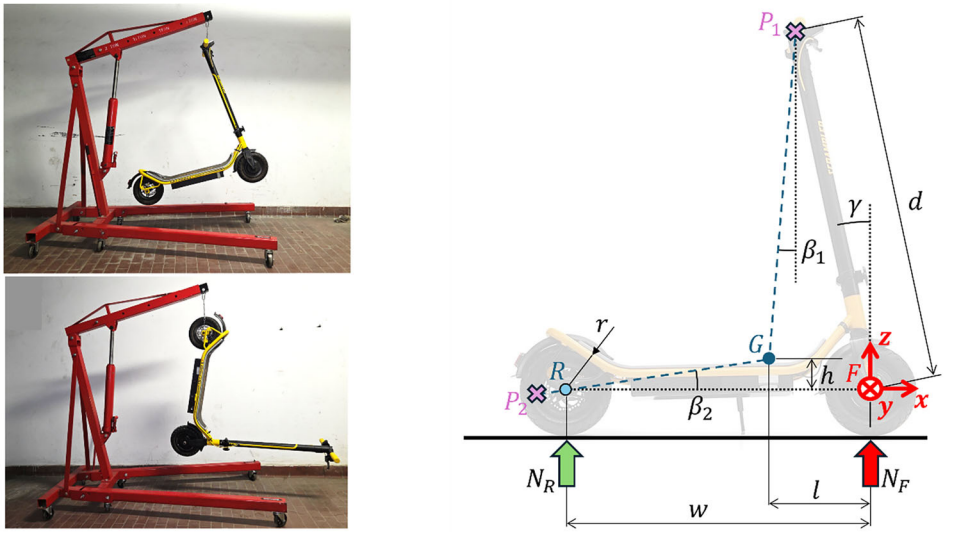

Figure 3. Centre of mass identification through the suspension method: experimental configuration (a) and schematic representation of the methodology employed to determine *G* coordinates (b).

2.1. Mass distribution

The mass distribution of each e-scooter is experimentally identified through a dedicated measurement procedure applied to all vehicles; for clarity, it is illustrated in Figure 3 with reference to V_2.

The coordinates of the vehicle centre of mass (G), expressed in the reference frame $\{F; \boldsymbol{x}, \boldsymbol{y}, \boldsymbol{z}\}$, are evaluated using the suspension method [60]. The e-scooter is suspended from the handlebar (P_1) and from the rear wheel rim (P_2), as shown in Figure 3(a). G is identified as the intersection of the two suspension lines, represented in Figure 3(b) as dashed blue segments and inclined by the angles β_1 and β_2 with respect to $\boldsymbol{z}$ and $\boldsymbol{x}$. To improve the robustness of the estimation, the position of G along $\boldsymbol{x}$ is independently verified using the static interface force measurement method [60]. In this configuration, two weight scales are placed under the front and rear wheels to measure the corresponding vertical reaction forces, N_F and N_R; the same procedure is repeated with the rider standing on the vehicle in the reference riding position as described in Section 3.1, allowing the load distribution on the tyres under steady-state operating conditions to be determined.

The complete mass-property characterisation is summarised in Table 2. The wheelbase and the steering column length are indicated by w and d, respectively, while γ represents the inclination of the steering column with respect to $\boldsymbol{z}$. The nominal tyre inflation pressure is indicated by p_a, and the tyre radius by r. The parameters l and h denote respectively the distance of G from F along $\boldsymbol{x}$ and $\boldsymbol{z}$.

2.2. Tyre radial stiffness

Tyre radial stiffness represents a key parameter governing the transmission of road-induced vibrations from the ground to the vehicle and, ultimately, to the rider. For this reason, the tyres of the three e-scooters are experimentally characterised under quasi-static conditions by varying the applied vertical load.

These tests are performed on an MTS QTest/10 Elite tensile/compression machine, as shown in Figure 4. The wheel hub is rigidly clamped to the fixed frame of the apparatus, while a load cell (10 kN full-scale range, accuracy of ± 0.01 N) and a compression plate are mounted on the moving crosshead. A digital dial gauge (accuracy of ± 1 µm) is used to verify that the deformation of the wheel and the clamping structure remain negligible with respect to the tyre deflection. Vertical load is applied in displacement control, while the corresponding reaction load L_z is recorded by the TestWorks 4 software at the sampling frequency of 10 Hz. All tyres are tested at their nominal pressure, monitored by an electronic air compressor (accuracy of ± 0.1 bar). During each test, the crosshead is lowered at a constant speed of 5 mm/min, resulting in an increasing vertical load from 0 to 1 kN. The upper load limit is selected based on the steady-state vertical wheel loads measured with the rider standing on the vehicle, reported in Table 2. Across the three vehicles, the maximum static operating load is observed at the rear wheel of V_2 and is equal to 570.5 N; therefore, the upper limit covers the full range of measured operating loads with a safety margin of approximately 75%. This range is considered sufficient for characterising the tyre radial stiffness in the load interval relevant to the subsequent regression analysis. This procedure is repeated five times to assess the repeatability of the results. Additional crosshead speeds (2 mm/min and 10 mm/min) are also tested to verify that the results are insensitive to the compression velocity. After verifying that wheel and fixture compliance are negligible, the crosshead displacement is taken as the tyre radial deflection δ. The resulting stiffness should therefore be interpreted as a quasi-static descriptor of the tyre radial compliance under representative operating loads, rather than as a complete dynamic tyre model. This assumption is sufficient for the scope of the present work because tyre stiffness is used as a comparative vehicle parameter in the regression analysis, not to reproduce the frequency-dependent tyre-road interaction during each run. In this sense, the measured radial stiffness provides a physically interpretable indicator of the tyre compliance available to filter road-induced excitations, while possible dynamic stiffness and damping effects are implicitly included in the measured on-road acceleration response.

The experimental relationship between L_z and δ for the three tyres is fitted using a fourth–order polynomial ($R^2 \approx 0.99$), as shown in the upper panel of Figure 4(b). The radial stiffness $\kappa(\delta)$ is then obtained by differentiating the fitted curves and is reported in the lower panel of Figure 4(b). Both V_2 and V_3 exhibit nearly identical stiffness behaviour over the investigated load range, whereas V_1 displays a higher radial stiffness over the full compression interval. For $\delta > 4$mm, κ of V_2 and V_3 remains almost constant, while V_1 shows a marked stiffening behaviour. For the sake of completeness, circular (◯) and square (□) markers in Figure 4(b) denote the operating conditions at the front and rear wheels, respectively, based on the corresponding steady-state vertical loads reported in Table 2.

The stiffness curve obtained for V_1 is consistent with the limited experimental data available in the literature for pneumatic e-scooter tyres. Asperti et al. [54,55] model the radial force-deflection relationship of an e-scooter tyre using a second-order polynomial,

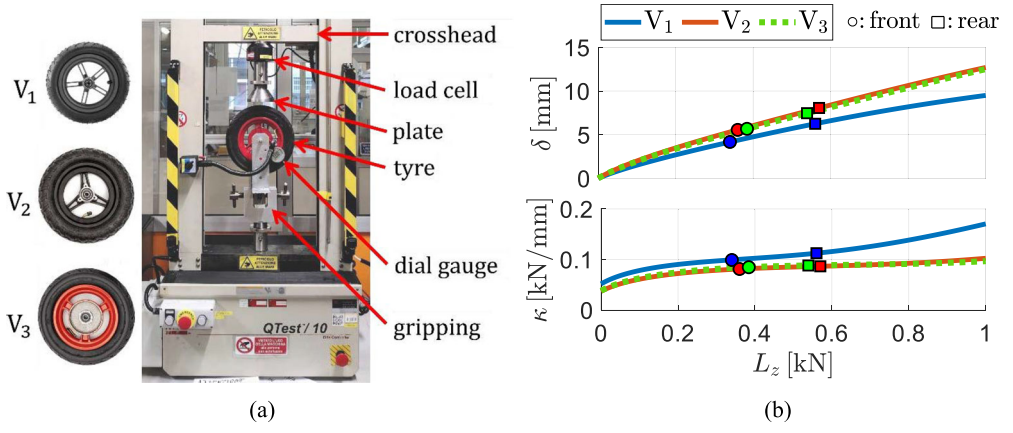

Figure 4. Tyres of the three e-scooters and experimental setup for radial stiffness characterisation (a), tyre deflection and radial stiffness as functions of vertical load (b).

and report that, at a pressure of 2.5 bar, the radial stiffness increases from approximately 0.05 kN/mm when $L_z = 0$ kN to about 0.1 kN/mm when $L_z \approx 0.8$ kN (corresponding to a deflection of $\delta = 10$mm). A similar order of magnitude is also reported in [61], where the average stiffness ranges between 0.09 kN/mm and 0.13 kN/mm for pneumatic e-scooter wheels, while substantially higher values are found for rigid wheels. These comparisons support the consistency of the measured stiffness values with previously published data and indicate that V_1 lies in the upper range of the stiffness values reported for pneumatic e-scooter tyres.

3. Experimental testing and signal processing

This section describes the on-road testing protocol, the measurement locations selected according to the standing riding posture, and the ISO-based signal-processing framework used for vibration filtering and discomfort evaluation.

3.1. Sensor setup and test protocol

The instrumentation adopted for the experimental campaign is shown in Figure 5(a). Two triaxial piezoelectric accelerometers (nominal sensitivity of 100 mV/g, range of ±50 g, and linearity of ±5% up to 5 kHz) are installed on each vehicle to measure the vibrations transmitted to the rider at the two human–machine interfaces associated with the standing posture: the foot-deck (D) and the hand-steering (S) interfaces. In accordance with ISO 2631–1 [22] and ISO 5349 [23], the accelerometers are positioned as close as practicable to the rider contact regions between the rider and the vehicle. To improve repeatability throughout the experimental campaign, the same mounting procedure is adopted for all vehicles. The accelerometers are rigidly fixed to the deck and steering structure using the same mechanical supports and adhesive interface. Their orientation is checked before each test to align the sensor axes with the vehicle reference frame shown in Figure 3. Small

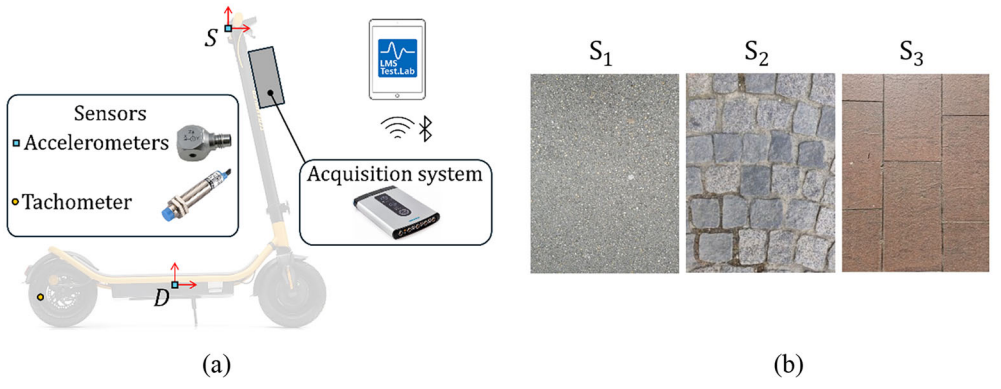

Figure 5. Layout of the experimental instrumentation (a) and road surfaces employed during the on-road tests (b).

residual mounting deviations may remain due to the local geometry of the deck and steering column; however, the same reference directions and installation procedure are used throughout the campaign to ensure consistency across all vehicles and test surfaces.

Vehicle speed is estimated by measuring the angular velocity of the driven wheel through an inductive proximity sensor (maximum detection distance of 4 mm, supply voltage between 4–36 V) repurposed as a tachometer. The sensor leverages the geometry of the wheel spokes and is powered by an external lithium-polymer (LiPo) 7.4 V battery (not shown in Figure 5(a)). In the two front-wheel-drive vehicles, the tachometer is installed on the rear wheel, whereas in the rear-wheel-drive vehicle it is mounted on the front wheel. All signals are synchronously acquired at a sampling frequency of 3200 Hz using a Siemens SCADAS XS data acquisition system housed in a protective case fixed to the steering column. Data acquisition and monitoring are managed through the Simcenter Testlab Scope App running on a tablet connected to the acquisition unit via Bluetooth.

Each acquisition starts from standstill conditions and is followed by a transient phase until reaching a target velocity. The rider then maintains a quasi-constant speed along a straight road segment of approximately 200 m on the selected surface, before decelerating to a stop, at which point the acquisition is terminated. During the analysed steady-speed segment, the rider maintains a straight trajectory without intentional steering manoeuvres, except for small corrective inputs required to preserve balance and lane position. This protocol is adopted to minimise vibration contributions associated with longitudinal and lateral vehicle dynamics, so that the measured response mainly reflects the vertical excitation induced by road surface irregularities. All tests are carried out under dry pavement conditions and in the absence of visible surface contamination. Runs affected by traffic interruptions, sudden manoeuvres, or non-stationary speed profiles are excluded from the steady-speed analysis. Environmental conditions are therefore controlled at the level required for a comparative on-road campaign, although no dedicated sensitivity analysis to temperature, wind or tyre thermal state was performed.

Three urban surfaces are considered, as shown in Figure 5(b): smooth asphalt (S_1), pavé (S_2), and a bike path (S_3). No direct road-profile measurements are performed in the present experimental campaign; therefore, the corresponding International Roughness

Index (IRI) values are not used as measured descriptors of the tested surfaces. However, reference values reported in the literature for comparable urban pavements indicate mean IRI values of approximately 2.7 m/km for smooth asphalt [58], 8.4 m/km for cobblestone/pavé surfaces [58,62,63], and 6.5 m/km for regular flagstone block pavements representative of modular pedestrian or cycling surfaces [62].

These values are used only to support the qualitative roughness ranking of the selected surfaces, with S_1 representing the smoothest condition, S_3 an intermediate condition, and S_2 the roughest one.

For each run, the steady-speed segment is performed at different velocities distributed within the range from 5 to 25 km/h. The lower bound of 5 km/h corresponds to the minimum speed setting available on the tested e-scooters, whereas the upper bound of 25 km/h reflects the speed limitation imposed by current regulations for this vehicle category. The aim is therefore not to test a fixed set of equally spaced speed levels, but to cover the usable operational speed range of each vehicle–surface combination. On the roughest surface, the highest velocities cannot always be reached or safely repeated, because the vibration severity may compromise rider safety and vehicle controllability. Therefore, the experimental dataset is representative of the practical operating range of each vehicle–surface combination rather than of a perfectly balanced full-factorial design.

All tests are conducted with the same rider, a healthy young adult male (height of 1.80 m, mass of 77.5 kg) with no known neurological or musculoskeletal disorders and with prior experience in e-scooter driving. The rider maintains a tandem stance throughout the experimental campaign, consistent with the guidelines reported in the literature [47,59]. The use of a single rider is intentionally adopted to control inter-subject variability and to isolate the effects of vehicle configuration, road surface and speed on the measured vibration response. This choice allows a more direct comparison among the tested e-scooters under repeatable rider-related conditions, while the implications for the generalisation of the results are discussed in Section 4.4. The experimental protocol was reviewed and approved by the Local Institutional Review Board. The participant provided informed written consent prior to participation. All procedures were conducted in accordance with the Declaration of Helsinki.

The same sensor setup and testing protocol are adopted for all vehicles. The number of runs performed for each combination of vehicle and surface is reported in Table 3. The number of repetitions is determined by combining repeatability requirements and practical constraints related to surface availability, traffic conditions, battery autonomy and rider safety. For each vehicle–surface combination, repeated runs are collected over the investigated speed range to ensure repeatability and to capture the main trends of the ISO-based discomfort indicators. As a consequence, the number of runs differs among vehicle–surface combinations, as reported in Table 3.

3.2. ISO-based vibration filtering and discomfort indicators

Figure 6 illustrates the procedure followed for processing the experimental signals. The measured wheel angular velocity signal, ω, is first low-pass filtered (cut-off frequency of 10 Hz) to remove the experimental noise and then used to estimate the vehicle longitudinal speed assuming negligible tyre slip, as shown in Figure 6(a). To ensure a homogeneous

Table 3. Number of experimental runs performed for each vehicle–surface combination.

		Surface		
		S_1	S_2	S_3
Vehicle	V_1	30	27	27
	V_2	57	71	33
	V_3	29	46	24

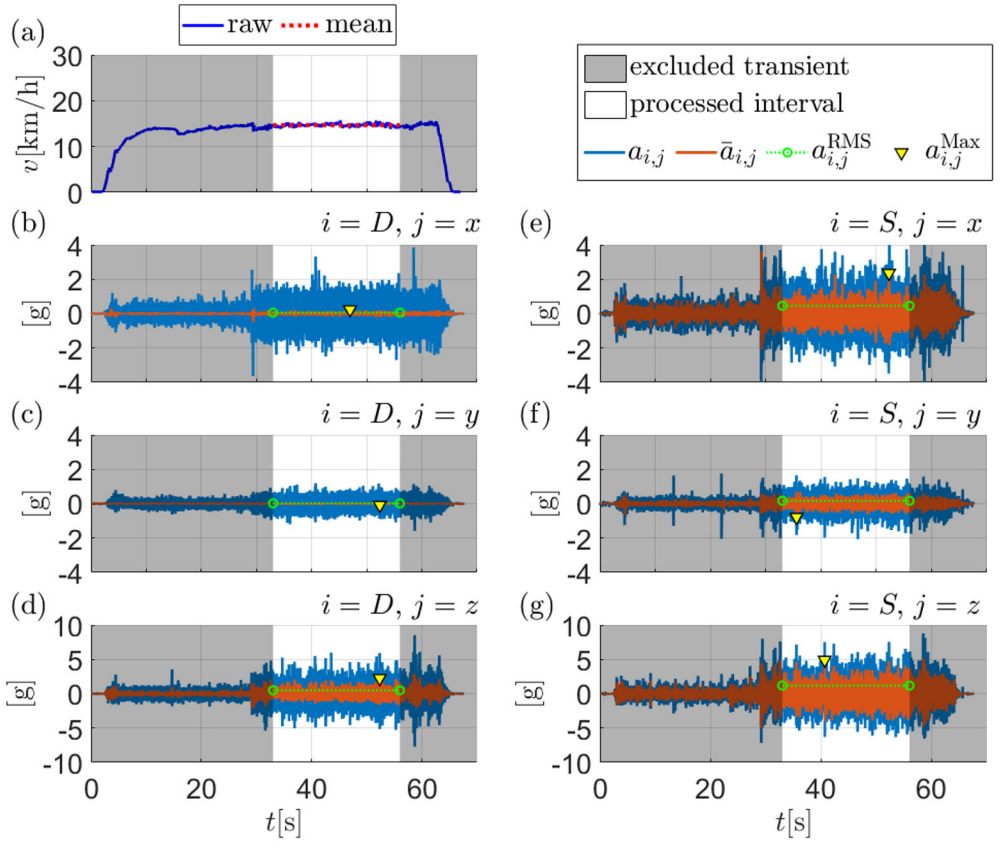

Figure 6. Data processing: vehicle velocity (a), raw and filtered acceleration components measured at the deck (b, c and d) and at the steering (e, f and g), root mean square and maximum values.

comparison among different test runs, the time histories of the accelerations are analysed only over road segments characterised by quasi-constant speed. Initial, settling, and final transient phases are therefore excluded from the analysis (shaded areas in grey in Figure 6(a–g)). This selection guarantees that the evaluated vibration levels are representative of steady riding conditions.

The raw acceleration signals $a_{ij}(t)$ (blue curves in Figure 6(b–g)) are processed in the time-domain by applying the frequency weighting function H_{ij} prescribed for comfort assessment. Specifically, ISO 2631–1 [22] weightings for WB vibrations in standing posture are adopted for signals measured at the foot-deck interface ($i = D$), while ISO 5349

[23] weightings for HT vibrations are applied to signals measured at the hand-steering interface ($i = S$). The standards are used here as general frameworks for the objective processing and comparison of human vibration exposure, rather than as e-scooter-specific comfort models. This distinction is particularly important because the standing posture adopted on e-scooters differs from the seated posture typically encountered in passenger vehicles: the back and pelvis contact interfaces are absent, and whole-body vibration transmission occurs mainly through the foot-deck interface, while the hand-steering interface is treated separately as hand-transmitted vibration. For each vibration direction, $j = \boldsymbol{x}, \boldsymbol{y}, \boldsymbol{z}$, the weighting operation yields a filtered acceleration signal $\bar{a}_{ij}$ (orange curve in Figure 6(b–g)), obtained as

$$\bar{a}_{ij}(t) = \mathcal{H}_{ij}\{a_{ij}(t)\} \qquad i = D, S \qquad j = \boldsymbol{x}, \boldsymbol{y}, \boldsymbol{z} \tag{1}$$

The operator $\mathcal{H}_{ij}\{\cdot\}$ denotes the time-domain implementation of the ISO weighting filter associated with the transfer function $H_{ij}(p)$, whose definition is reported in Appendix A. From the filtered signals, two basic descriptors are extracted. The root mean square (RMS) value (green dotted lines in Figure 6(b–g)),

$$a_{ij}^{\mathrm{RMS}} = \sqrt{\frac{1}{T}\int_0^T \bar{a}_{ij}^2(t)dt} \qquad i = D, S \qquad j = \boldsymbol{x}, \boldsymbol{y}, \boldsymbol{z} \tag{2}$$

represents the overall vibration energy, while the maximum (Max) absolute value (yellow downward triangles in Figure 6(b–g)),

$$a_{ij}^{\mathrm{Max}} = \underset{t\in[0,T]}{\mathrm{Max}} |\bar{a}_{ij}(t)| \qquad i = D, S \qquad j = \boldsymbol{x}, \boldsymbol{y}, \boldsymbol{z} \tag{3}$$

captures peak events occurring during the run. Here t denotes the time variable, while T is the duration of the segment after excluding the initial, settling and final transient phases.

These quantities are combined to derive two synthetic indicators. The first is a discomfort index, DI_i, obtained by combining the RMS components through the directional multiplying factors k_{ij} prescribed by the standards,

$$\mathrm{DI}_i = \sqrt{\sum_j \left(k_{ij} a_{ij}^{\mathrm{RMS}}\right)^2} \qquad i = D, S \qquad j = \boldsymbol{x}, \boldsymbol{y}, \boldsymbol{z} \tag{4}$$

This index provides an objective benchmark for comparing different vehicles, surfaces and operating conditions. The second indicator is the crest factor,

$$\mathrm{CF}_{ij} = \frac{a_{ij}^{\mathrm{Max}}}{a_{ij}^{\mathrm{RMS}}} \qquad i = D, S \qquad j = \boldsymbol{x}, \boldsymbol{y}, \boldsymbol{z} \tag{5}$$

which characterises the relative prominence of impulsive events in each vibration direction. According to ISO recommendations, the RMS-based evaluation is considered appropriate when $\mathrm{CF}_{ij} \leq 9$. Further details on the definition of the weighting filters are reported in Appendix A for completeness.

3.3. Influence of vehicle and operating parameters on ride quality

A regression-based analysis is carried out to investigate the dominant dependencies between the discomfort index and selected vehicle- and test-related parameters. The analysis is intentionally limited in scope and is not intended as a general predictive model for arbitrary e-scooter configurations; rather, it is used to support the physical interpretation of the experimental trends observed across different vehicles, road surfaces and riding conditions.

The regression analysis is performed using data collected with V_1 and V_2 on S_1 and S_2 (model identification). This choice defines four vehicle-surface identification cases. The measurements obtained with V_3, as well as those collected on S_3, are instead reserved for validation. Since the number of available observations is not uniformly distributed among vehicles and surfaces, a Weighted Least–Squares (WLS) approach is adopted to ensure a balanced contribution from each vehicle-surface combination. The imbalance arises from practical constraints of the on-road campaign and from the need to ensure rider safety under particularly severe vibration conditions. Specifically, not all target speeds could be safely repeated for every vehicle–surface combination. The WLS formulation is therefore introduced to prevent cases with a larger number of observations from dominating the identification process. By assigning the same overall weight to each vehicle–surface combination, the regression preserves the relative contribution of the different configurations despite the unequal number of runs.

For each human–machine interface ($i = D, S$), the coefficient vector $\boldsymbol{\alpha}_i = [\alpha_{i,1}, \ldots, \alpha_{i,n_r}]^t$ is obtained by solving

$$\boldsymbol{\alpha}_i = \arg\min_{\hat{\boldsymbol{\alpha}}_i} \sum_{e=1}^{E} w_e (\mathrm{DI}_{i,e} - \boldsymbol{u}_e^t \hat{\boldsymbol{\alpha}}_i)^2 \qquad i = D, S \tag{6}$$

where E is the total number of observations, $\mathrm{DI}_{i,e}$ denotes the measured discomfort index at interface i for observation e, $\boldsymbol{u}_e \in \mathbb{R}^{n_r}$ is the regressor vector describing the corresponding vehicle and test conditions, and w_e are the weighting factors. w_e are defined to ensure equal overall contribution from each vehicle-surface case, as shown in

$$\sum_{e:\, c(e)=c} w_e = \sum_{e:\, c(e)=c} \frac{1}{n_c} = 1 \qquad c = 1, \ldots, 4 \tag{7}$$

where $c(e) \in \{1, \ldots, 4\}$ identifies the vehicle-surface case associated with observation e in the identification dataset, and n_c is the number of tests available for case c.

The set of regressors $\boldsymbol{u}_e$ involves vehicle and test–related parameters, as well as their mutual interactions. Specifically, the parameters under analysis include:

- vehicle speed (v);
- road surface type, represented by the coefficient $q_R \in \{0, 1\}$, with $q_R = 0$ for S_1 and $q_R = 1$ for S_2;
- average operational tyre stiffness κ_0, defined as a vertical-load-weighted combination of front and rear tyre stiffness under steady-state conditions (Figure 4(b)), as expressed in

$$\kappa_0 = \frac{\kappa_F N_F + \kappa_R N_R}{N_F + N_R} \tag{8}$$

- unloaded tyre radius (r);
- vehicle geometries, i.e. the wheelbase (w) and the steering column length (d);
- mass (m) and centre of mass location (l, h).

The selection of the final regressors is driven by the objective of maintaining model parsimony and physical interpretability, rather than maximising fitting accuracy. Candidate variables are first identified based on observed experimental trends and are subsequently screened through diagnostic checks aimed at excluding spurious correlations, collinearity effects and inadequate functional forms [64,65].

Using the selected regressors and the corresponding estimated coefficients, the discomfort index is reconstructed for each observation and compared with the corresponding experimental value. The overall goodness of fit is quantified through the coefficient of determination R^2, while the validation of the regression model is achieved in two distinct steps:

- estimation of q_R on S_3 through a second WLS procedure;
- computation of the Normalised Root Mean Square Error (NRMSE) between measured and predicted discomfort index, clustering the dataset according to vehicle (V_1, V_2, and V_3) and road surface (S_1, S_2, and S_3).

4. Results and discussion

This section presents the experimental results and discusses their regression-based interpretation, practical implications and main limitations.

4.1. Ride comfort assessment

Figure 7 compares the three vehicles in terms of discomfort index (DI_i) as a function of the testing velocity v for asphalt (S_1) and pavé (S_2). Results obtained at the foot-deck interface ($i = D$) are reported in Figure 7, while Figure 8 shows the corresponding values at the hand-steering interface ($i = S$). Colours and markers are used consistently across the panels to distinguish vehicles and road surfaces: cyan, green and magenta are used for V_1, V_2, and V_3, while circles (◯) and squares (□) denote tests on S_1 and S_2. In Figure 7, the background colour bands indicate the ride quality regions suggested in ISO 2631-1 [22] (see Appendix A for details). These comfort regions are used as reference bands for interpreting the severity of foot-deck vibration exposure, rather than as absolute thresholds of perceived comfort for all e-scooter riders. For the sake of clarity, DI_D and DI_S detected on the bike path (S_3) are reported in Appendix B, in Figures A1 and A2.

For all vehicles and measurement locations, the discomfort index generally increases with vehicle speed, confirming the dominant role of speed in amplifying road-induced vibrations. On pavé, both DI_D and DI_S for V_2 and V_3 increase up to approximately $v =$ 20 km/h and then tend to level off. From a physical interpretation standpoint, this trend should not be regarded as a reduction in road excitation at higher speeds. Rather, it may result from the combined effects of ISO frequency weighting and changes in rider–vehicle

interaction under severe vibration conditions. As speed increases, the spatial irregularities of the pavé surface are shifted toward higher temporal excitation frequencies, causing part of the vibration spectrum to fall outside the frequency range where the ISO weighting functions are most sensitive. At the same time, severe vibration levels may induce small adaptations of the rider posture, knee compliance, grip force and foot-deck contact conditions, thereby modifying the effective transmission path between the vehicle and the body. It is worth noting that V_1 cannot be tested on pavé above 19 km/h because the vibration levels become excessive and compromise rider safety.

For a given speed, pavé systematically produces substantially higher comfort degradation than asphalt at both interfaces, highlighting the strong influence of surface roughness on vibration transmission. At the foot-deck interface, discomfort levels on pavé are typically 4.5 to 6 times larger than those measured on asphalt, while at the hand-steering interface the increase ranges from approximately 3.5 to 8 times, depending on the vehicle. Beyond the overall increase in vibration severity, pavé surfaces also enhance the ability

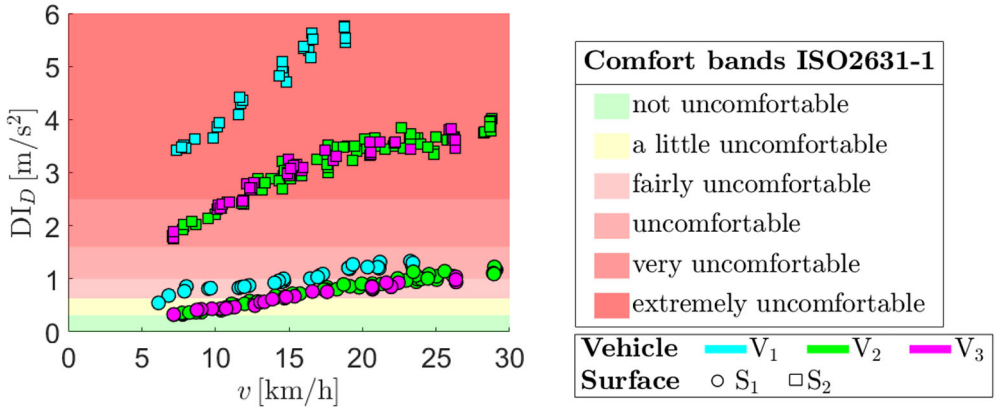

Figure 7. Discomfort index evaluated at the foot-deck interface for the three vehicles on asphalt and pavé surfaces for different vehicle velocities.

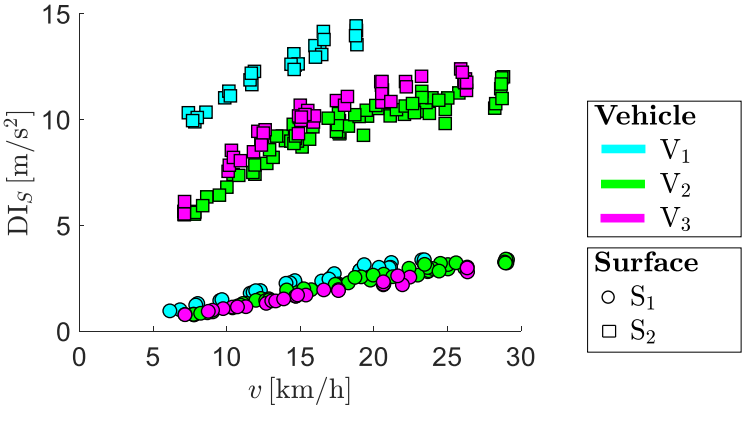

Figure 8. Discomfort index evaluated at the hand-steering interface for the three vehicles on asphalt and pavé surfaces for different vehicle velocities.

to discriminate between different e-scooter layouts. On asphalt, the three vehicles show relatively close DI_i values, particularly at low and moderate speeds. In contrast, on pavé the separation among vehicles becomes more pronounced across the entire speed range, indicating that rough surfaces magnify the effect of design differences on the transmitted vibrations. Among the tested models, V_1 exhibits the worst comfort across the entire speed range and at both measurement locations. V_2 and V_3 show similar behaviour at the foot-deck interface for both surfaces and similar values at the hand-steering interface on asphalt, while V_2 is slightly more comfortable than V_3 on pavé at the steering.

Considering the comfort regions defined by ISO 2631-1 reported in Figure 7, asphalt runs remain predominantly within mild to moderate vibration exposure over the investigated speed range ($DI_D < 1.4 m/s^2$). In contrast, pavé results fall almost entirely within the most severe ISO 2631-1 reference comfort region ($DI_D > 1.8 m/s^2$), emphasising that highly irregular surfaces, e.g. S_2, impose vibration levels associated with severe discomfort according to the ISO 2631-1 reference band. Bike path represents an intermediate condition between asphalt and pavé. Both at the foot-deck and hand–steering interfaces, discomfort levels on the bike path surface are higher than those measured on asphalt but remain significantly lower than those observed on pavé, further confirming the sensitivity of e-scooter comfort to surface quality.

Figure 9 summarises the crest factor values (CF_i) evaluated at the foot-deck and hand-steering interfaces for all vehicles and surfaces. Since no clear dependence on vehicle speed is observed, crest factors are averaged for each vibration direction ($\boldsymbol{x}$, $\boldsymbol{y}$, and $\boldsymbol{z}$) and are reported together with their dispersion. Figure 9(a)–(c) show the crest factor at the foot-deck interface ($i = D$), while Figure 9(d)–(f) present the corresponding values at the hand–steering interface ($i = S$). Figure 9(a) and (d) refer to asphalt (S_1), Figure 9(b) and (e) correspond to pavé (S_2), and 9(c) and 9(f) show the results from the bike path (S_3). In each plot, the cross symbol indicates the mean crest factor (μ), the error bar represents the standard deviation ($\pm\sigma$), the downward triangle marks the maximum values, and the upward triangle denotes the minimum values. Colours are used consistently to distinguish the three vibration directions: blue for the $\boldsymbol{x}$-axis, orange for the $\boldsymbol{y}$-axis, and yellow for the $\boldsymbol{z}$-axis.

Across all vehicles, directions and surfaces, the mean crest factors, together with their standard deviations, remain below the reference threshold of $CF = 9$ at both human-vehicle interfaces, supporting the use of the RMS-based indicators adopted in this study. The values of CF_D are comparable among the three vehicles on all surfaces, indicating similar overall peak–to–RMS characteristics at the foot. However, the maximum values occasionally exceed the threshold on asphalt, particularly for V_1 in the $\boldsymbol{x}$ and $\boldsymbol{z}$ directions ($CF_{Dx} = 9.6$, $CF_{Dz} = 12.0$) and for V_2 in the $\boldsymbol{x}$ direction ($CF_{Dx} = 10.0$).

In general, CF exhibits a larger dispersion on asphalt and on the bike path than on pavé. This behaviour arises from the lower weighted RMS typically measured, which increases the prominence of peak accelerations in the crest factor ratio (Eq. (5)). Conversely, on pavé the higher overall vibration levels tend to mask individual peaks, resulting in more compact distributions and smaller standard deviations. Comparing the two measurement locations, higher crest factors are generally observed at the hand-steering interface than at the foot-deck interface. This evidence can be attributed to geometric and structural amplification effects: the steering point is located farther from the ground and therefore is more sensitive

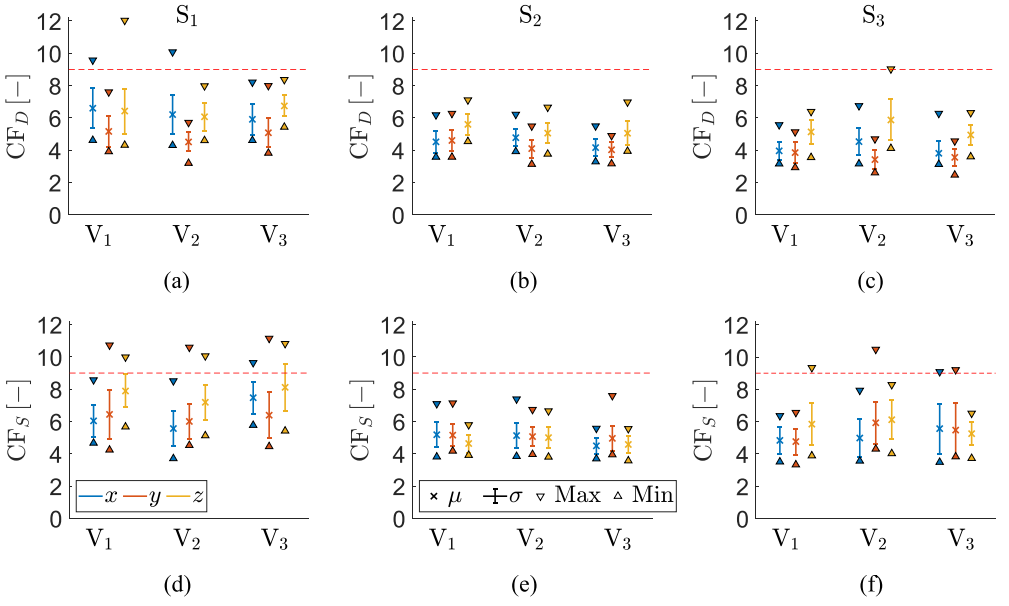

Figure 9. Average, standard deviation, maximum and minimum values of the crest factor evaluated at the foot-deck (a, b, and c) and hand-steering (d, e, and f) interfaces for the three vehicles on asphalt (a and d), pavé (b and e), and bike path (c and f) surfaces.

to pitch dynamics (rotation around the y-axis of the vehicle), while the flexibility of the steering column and possible joint clearances can locally amplify peak accelerations.

4.2. Regression–based interpretation of ride comfort

To support a physical interpretation of the ride comfort assessment, a regression analysis is introduced. The objective of this analysis is not to provide a general-purpose predictive tool for arbitrary e-scooter configuration, but rather to quantify the relative contribution of selected vehicle characteristics and operating parameters to the experimentally observed discomfort indices. Consistently with this goal, the model formulation prioritises simplicity and physical interpretability over the maximisation of fitting accuracy.

4.2.1. Regression formulation and physical interpretation

The regression function that is selected to describe DI_i at the human–vehicle interface i is expressed as

$$\mathrm{DI}_i = \alpha_{i,1} + \alpha_{i,2}\kappa_0 + \alpha_{i,3}q_R + \alpha_{i,4}q_R\kappa_0 + \alpha_{i,5}v + \alpha_{i,6}q_R\kappa_0 v + \alpha_{i,7}q_R v^2 \tag{9}$$

The model structure reflects the experimental evidence observed in Figures 7 and 8, with vehicle speed v emerging as the dominant explanatory variable for both interfaces. Among the remaining parameters, the road-surface coefficient q_R and the average operational tyre stiffness κ_0 exhibit the most significant contributions.

For asphalt runs ($q_R = 0$), the regression reduces to a linear dependence on vehicle speed. In this condition, DI_i increases with a constant rate, reflecting the progressive amplification of broadband vibrations induced by rolling excitation. The baseline level of the

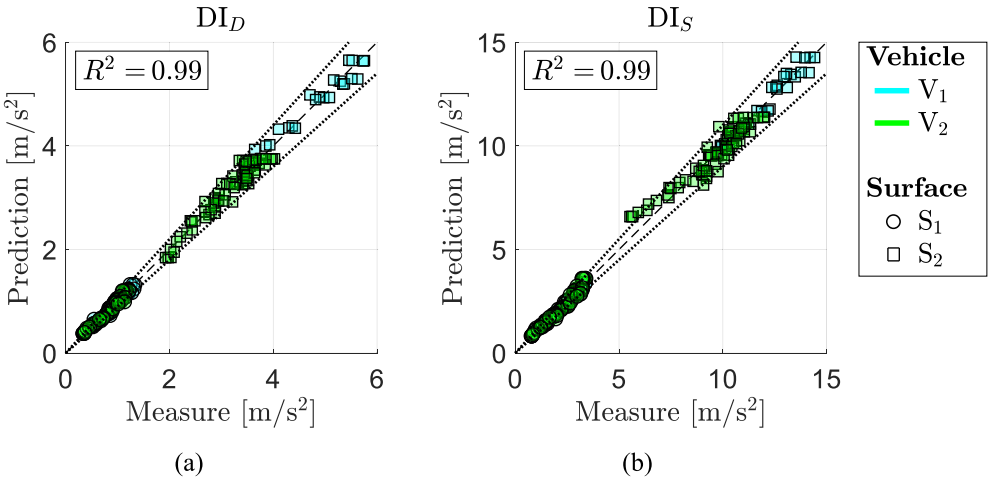

Figure 10. Predicted versus measured discomfort index evaluated at the foot-deck (a) and hand-steering (b) interfaces for V_1 and V_2 on asphalt and pavé surfaces.

linear trend depends on κ_0: stiffer tyres transmit larger accelerations to the vehicle structure and, consequently, to the rider, leading to higher baseline discomfort levels.

The effect of the road surface is primarily introduced through the activation of the terms associated with q_R, which shifts DI_i upwards when transitioning from asphalt to pavé ($q_R = 1$). This offset captures the higher excitation energy associated with the irregular cobblestone surface. The mixed terms $q_R\kappa_0$ and $q_R\kappa_0 v$ indicate that, on pavé, discomfort not only increases in magnitude but also exhibits a higher sensitivity to speed, consistently with the experimental trends observed in Section 4.1. This result suggests that stiffer tyres exacerbate the transmission of road-induced vibrations on highly irregular surfaces, particularly at higher velocities, where both excitation amplitude and frequency content increase. Finally, the quadratic term $q_R v^2$, which is non-zero on the pavé surface, introduces a nonlinear dependence on speed. This contribution reflects the increasingly complex dynamic response of the e-scooter–rider system over irregular surfaces, where changes in speed modify not only vibration amplitude but also the distribution of excitation frequencies. For the sake of compactness, the regression parameters and the estimated coefficients $\boldsymbol{\alpha}_i$ are reported in Tables A4 and A5, respectively.

4.2.2. Model performance and validation

Figure 10 compares DI_i predicted by the regression model (Eq. (9)) with the corresponding experimental values at the foot-deck (Figure 10(a)) and hand-steering (Figure 10(b)) interfaces. Colours differentiate the vehicles, whereas marker shapes correspond to the different road surfaces. The dashed line represents the ideal one-to-one correspondence between predicted and measured values while black dotted lines indicate a $\pm 10\%$ tolerance band.

For both interfaces, the data points are distributed close to the one-to-one line, indicating that the model captures the main trends observed in the identification dataset.

To further assess the robustness of the proposed regression model, the formulation is tested against data collected on vehicle V_3, which is deliberately excluded from the identification phase: Figure 11 compares the predicted and measured discomfort indices at

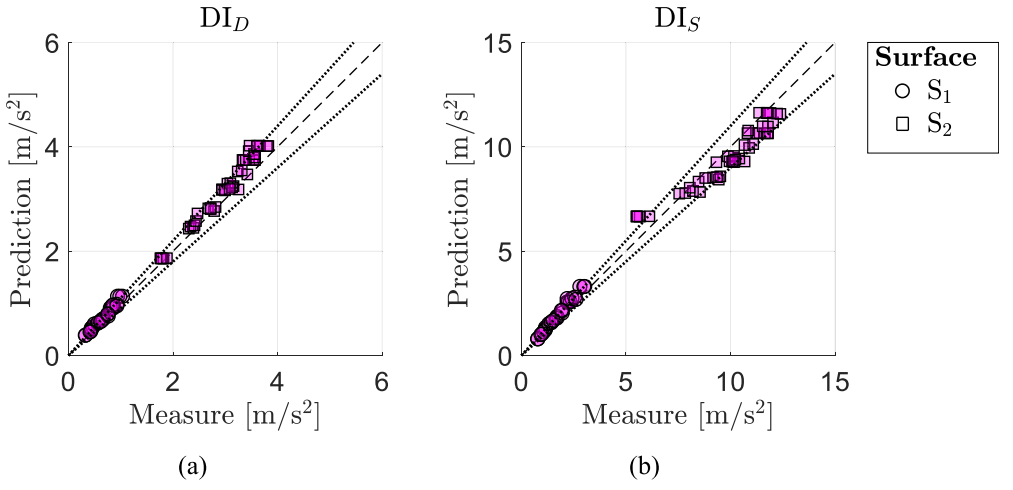

Figure 11. Predicted versus measured discomfort index evaluated at the foot-deck (a) and hand-steering (b) interfaces for V_3 on asphalt and pavé surfaces.

the foot-deck and hand-steering interfaces on asphalt and pavé surfaces using the same regression coefficients identified from the V_1-V_2datasets.

Despite the absence of vehicle–specific fitting, the predicted DI_i values show good agreement with the experimental measurements for both interfaces and road surfaces. Data points remain reasonably close to the ideal one-to-one correspondence line, indicating that the regression model retains its descriptive capability even when applied to a vehicle not used during identification. Slightly larger deviations are observed at the hand-steering interface, particularly on pavé, although the overall trends with speed and road surface are correctly reproduced.

A further validation of the regression framework is carried out by considering the bike path surface (S_3), which is not included in the model identification phase. In this analysis, all regression coefficients identified from the asphalt and pavé datasets are kept fixed. The only surface-related variable introduced for the bike path is q_R, which is estimated through a WLS procedure using the experimental data collected on S_3 with all three vehicles. No additional model coefficients or interaction terms are re-identified. Figure 12 compares the corresponding predicted and measured discomfort indices at the foot-deck and hand-steering interfaces.

Despite the scalar parametrisation of surface condition, the model demonstrates good agreement with the experimental evidence. The larger dispersion observed in the bike path results can be explained by the spatial variability of the surface excitation. For asphalt and pavé (S_1 and S_2), all acquisitions are performed along the same road segment, ensuring a high level of repeatability in the realised roughness profile. In contrast, the tests on S_3 are carried out on different locations of the same cycling infrastructure. Although the surface type is nominally the same, local variations in pavement condition and construction quality lead to different realisations of the roughness profile, which directly affects the transmitted vibrations. This behaviour is consistent with the simplified representation of road roughness adopted in the regression model, where the complex spatial characteristics of the surface are condensed into a single scalar parameter.

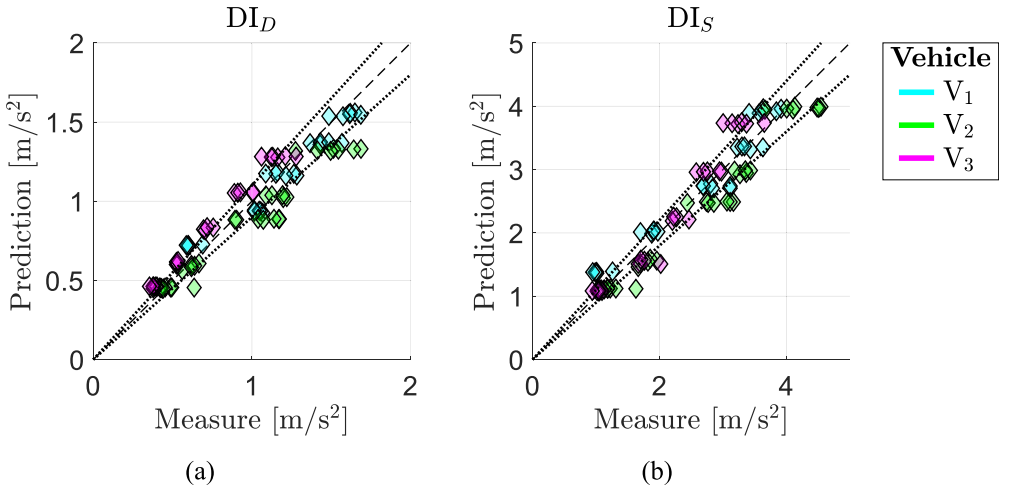

Figure 12. Predicted versus measured discomfort index evaluated at the foot-deck (a) and hand-steering (b) interfaces for the three vehicles on the bike path.

Table 4. Normalised root mean square error between predicted and measured discomfort indices at the foot-deck and hand-steering interfaces, grouped by vehicle and road surface.

		NRMSE	
Cluster		*D*	*S*
Vehicle	V_1	0.04	0.034
	V_2	0.051	0.061
	V_3	0.094	0.088
Surface	S_1	0.073	0.082
	S_2	0.053	0.055
	S_3	0.13	0.12

Finally, to quantitatively assess the predictive accuracy of the regression model, NRMSE values between predicted and measured DI_i are computed. The NRMSEs are reported in Table 4, clustering the results according to vehicle (V_1, V_2, and V_3) and road surface (S_1, S_2, and S_3), and separately for foot-deck (*D*) and hand-steering (*S*).

For all clusters, NRMSEs always remain below 0.1 except for S_3, indicating a generally good predictive capability of the regression model. As expected, the lowest errors are obtained for V_1 and V_2 which are used in the model identification phase. Slightly higher errors are observed for V_3 at both interfaces, consistently with its role as an external validation case.

When clustering the data by road surface, marginally lower NRMSE values are observed on pavé than on asphalt for both interfaces. This behaviour can be attributed to the higher vibration levels measured on pavé, which reduce the relative impact of local discrepancies between predicted and measured values when normalised by the signal magnitude. Conversely, on asphalt the lower overall discomfort levels amplify the effect of small absolute prediction errors, leading to slightly larger normalised errors. Higher NRMSE values are

also observed for the bike path surface (S_3): this behaviour is consistent with the trends discussed in Figure 12 and can be primarily attributed to the spatial variability of the excitation along the cycling infrastructure.

Overall, the error distribution reported in Table 4 confirms that the regression model captures the dominant experimental trends governing vibration-induced comfort degradation across vehicles and surfaces. The physical trends observed in the present study are also consistent with previous experimental evidence on e-scooter and bicycle vibration comfort. Asperti et al. [58] identify road quality and vehicle speed as the most influential parameters governing e-scooter vertical dynamics and frequency-weighted vibration exposure. The observed sensitivity to road surface is also consistent with the comparison between e-scooters and e-bikes reported in [52,53], where e-scooters exhibited higher vibration magnitudes and a stronger dependence on path, user and speed factors than e-bikes. From the bicycle literature, similar dependencies between vibration exposure, pavement condition, speed and tyre–pavement interaction have been reported in [41,42]. However, the present results indicate that these mechanisms are amplified in e-scooters because of the smaller wheel diameter, limited passive isolation and standing rider posture, which reduce the available vibration attenuation between the road input and the rider contact interfaces.

To further support the robustness of the regression-based interpretation, diagnostic checks are performed on the final WLS models. For the sake of compactness, the corresponding results are reported in Appendix C. The correlation matrix (Table A6) indicates that the strongest correlations are localised in the road-activated interaction terms, i.e. $q_R\kappa_0$, $q_R\kappa_0 v$, and $q_R v^2$. This behaviour is expected, since these terms are activated only on rough-surface conditions ($q_R > 0$) while in the present analysis the road-surface coefficient q_R can assume a limited number of discrete values. Conversely, the main physical regressors, namely speed v and average tyre stiffness κ_0, do not show strong mutual correlation, supporting the physical interpretability of the selected model structure. The global F-tests (reported in Table A7) confirm that the WLS models are statistically significant, with $F > 6 \cdot 10^3$ and $p < 10^{-3}$ for both foot-deck and hand-steering cases. The individual coefficient tests also indicate that all retained predictors are statistically different from zero within the fitted models ($p < 10^{-3}$). Nevertheless, the Breusch–Pagan test (reported in Table A8) rejects the null hypothesis of homoscedastic residuals for both interfaces ($LM > 30$). This result is consistent with the experimental dataset, which combines operating conditions characterised by markedly different vibration amplitudes, especially asphalt and pavé. Accordingly, the regression model should be interpreted as a compact and physically motivated description of the dominant experimental trends, rather than as a fully inferential model based on homoscedastic residuals.

4.3. Practical implications for e-scooter design and deployment

The experimental and regression-based results provide practical indications for the design, operation and deployment of electric kick scooters. From a design perspective, vibration transmission should be explicitly considered during vehicle development. Tyre selection represents a critical parameter, since more compliant tyres and larger wheels may reduce the vibration levels transmitted to the rider, especially on irregular pavements. Similarly,

the adoption of effective suspension elements may help mitigate the severe vibration exposure observed on rough surfaces, encouraging further investigation of suspension design and tuning strategies specifically tailored to the dynamic characteristics of compact e-scooters. From an operational perspective, the dominant influence of speed suggests that regulations should not rely solely on a uniform maximum speed limit but should also account for local pavement conditions. On highly irregular pavements, reducing the permitted speed may improve not only comfort, but also controllability and operational safety. Low-cost inertial measurement units integrated into the vehicle could be used to monitor vibration levels during operation and to support adaptive strategies in which the maximum speed is automatically reduced when excessive vibration exposure is detected. For shared micromobility fleets, which are often already equipped with GPS-based localisation systems, this approach could be complemented by geofencing strategies that implement area-specific speed limits based on pavement quality, road category, or predefined urban zones.

4.4. Limitations and scope of the study

The present study is designed to provide a controlled and reproducible comparison of vibration-induced ride comfort among different e-scooter configurations, rather than a complete representation of all real-world riding conditions. Accordingly, the analysis deliberately focuses on objective ISO-based indicators evaluated at the two main rider-vehicle contact interfaces, i.e. the foot-deck and hand-steering interfaces. This approach enables a standardised and physically interpretable comparison among vehicles, surfaces and speeds, but it does not include subjective rider ratings, which depend on individual sensitivity, expectation, confidence and riding experience.

A first limitation concerns the use of a single rider throughout the experimental campaign. This choice is intentionally adopted to reduce inter-subject variability and isolate the effects of vehicle layout, road surface and speed on the measured vibration response. However, rider-related factors may substantially affect the coupled rider-vehicle dynamics and the resulting vibration transmission. In particular, body mass modifies the static wheel loads and tyre operating conditions, while posture, joint compliance, riding style and experience influence the mechanical impedance of the rider-vehicle system. Therefore, the reported results should be interpreted as a controlled comparison among vehicle configurations under a fixed rider condition, rather than as a direct description of the variability expected across the broader e-scooter user population.

The experimental protocol also represents a simplified subset of urban riding. The tests are performed on approximately straight 200m road segments, and only quasi-steady-speed portions are retained for the ISO-based analysis. This approach allows the influence of vehicle speed and road-induced vertical excitation to be investigated while limiting the confounding effects associated with acceleration, braking, cornering, obstacle avoidance and traffic interactions. As a consequence, the results are representative of controlled steady-speed riding on homogeneous straight surfaces, but they should not be interpreted as a complete estimate of vibration exposure over full urban trips, where route length, transient manoeuvres, repeated stops, rider adaptation and traffic conditions may alter both excitation input and rider–vehicle coupling.

A further limitation concerns the simplified representation of the mechanical transmission paths between the road input and the rider contact interfaces. The regression model includes compact descriptors of vehicle layout, road surface and speed, but it does not explicitly account for structural compliance of the steering column, joint clearances, damping properties of the frame and suspension elements, or frequency-dependent rider biomechanics. As a consequence, part of the residual discrepancies, especially those observed at the hand-steering interface, may originate from unmodelled structural and biomechanical effects rather than from the selected regressors alone.

The vehicle and road samples should also be interpreted within the scope of a controlled experimental comparison. Although the three selected e-scooters differ in wheel size, tyre characteristics, mass distribution and suspension layout, they cannot represent the full range of commercial designs currently available. Similarly, the three road surfaces are treated as representative urban pavement categories, and the regression model condenses surface effects into a compact scalar coefficient. This formulation supports a parsimonious interpretation of the dominant experimental trends, but it does not replace an independent quantitative characterisation of road roughness, such as profile-based PSD or IRI indicators. The higher prediction errors observed on the bike path surface are consistent with this limitation, since local spatial variability of the pavement cannot be fully captured by a single surface descriptor.

A specific methodological aspect concerns the interpretation of ISO-based comfort references for e-scooter riding. ISO 2631-1 and ISO 5349 provide established procedures for processing whole-body and hand-transmitted vibrations, but they are not developed specifically for compact standing vehicles. In e-scooters, the absence of seat, backrest and pelvis contact interfaces makes the foot-deck interaction the dominant path for whole-body vibration transmission, while the hand-steering interface must be considered separately. Moreover, the analysed runs correspond to short steady-speed exposures, whereas perceived comfort in daily use may depend on cumulative exposure and trip duration. For these reasons, the ISO-based discomfort indicators and the ISO 2631-1 comfort bands are used here as reference metrics for objective comparison, not as absolute predictors of perceived comfort for all e-scooter riders.

Although the main experimental trends are supported by repeated runs, a complete uncertainty propagation analysis is not included in the present work. The uncertainty affecting the ISO-based discomfort indices and crest factors may originate from accelerometer sensitivity and linearity, residual sensor mounting misalignment, data acquisition resolution, vehicle-speed estimation from the wheel tachometer, and the selection of the steady-speed analysis window. In addition, the on-road nature of the campaign introduces experimental variability related to the exact trajectory followed during each run, the local section of pavement actually travelled, small residual speed fluctuations, and possible variations in the rider's posture and contact conditions. These effects are addressed by performing repeated runs for each vehicle-surface combination and analysing the resulting data dispersion, rather than by applying a formal error-propagation framework.

Finally, tyre radial stiffness is characterised under quasi-static loading conditions and used as a compact design parameter in the regression model. This assumption is appropriate for comparing the relative compliance of the tested vehicles under representative vertical loads, but it does not capture the full dynamic behaviour of the tyres when rolling

over irregular surfaces. Dynamic stiffness, damping, contact-patch effects and frequency-dependent phenomena may contribute to the measured vibration response but are not explicitly represented by the stiffness parameter used here.

5. Conclusions

This work presented an experimental assessment of vibration-induced ride comfort in commercial electric kick scooters under controlled steady-speed urban riding conditions. Three vehicles with different layouts were tested on three representative pavement surfaces, and dedicated laboratory tests were performed to characterise vehicle mass properties and tyre radial stiffness. Accelerations transmitted to the rider at the foot-deck and hand-steering interfaces were processed in accordance with ISO 2631-1 and ISO 5349, providing an objective, standardised, and interface-specific comparison of whole-body and hand-transmitted vibration exposure.

The ISO-based analysis showed that surface type has a major effect on rider vibration exposure. Compared with asphalt, pavé increased the discomfort index by approximately 4.5–6 times at the foot-deck interface and by approximately 3.5–8 times at the hand-steering interface, depending on the vehicle. While asphalt generally resulted in mild to moderate vibration exposure at the foot-deck interface, pavé conditions almost always fell within the most severe ISO 2631-1 reference comfort region. For V_1, the vibration levels on pavé were sufficiently high to preclude safe testing above 19km/h, indicating that severe vibration exposure may also affect rider controllability and the practical speed range.

Vehicle speed emerged as the dominant operational parameter governing vibration-induced discomfort across all vehicles and surfaces. Tyre radial stiffness also played a relevant role, since the vehicle with the highest operational stiffness consistently exhibited higher vibration levels, especially on irregular surfaces. The proposed regression model provided a compact and physically interpretable description of these trends, linking the discomfort indicators to speed, road surface condition and tyre stiffness. Despite its simplified structure, the model showed good agreement with the experimental data, with NRMSE values below 0.1 for all vehicle- and surface-based clusters except for those associated with the bike path surface, for which larger errors were mainly associated with the spatial variability of the pavement.

Overall, the results indicate that e-scooter ride comfort is governed by a limited set of dominant factors whose combined effects can rapidly lead to vibration levels incompatible with comfortable and controllable riding on highly irregular urban surfaces. These findings support the need to consider vibration transmission as a design and deployment criterion, promoting more compliant tyres, effective suspension or vibration isolation solutions, and surface-dependent speed management on routes intended for e-scooter use.

The present study focused on steady-speed riding along straight road segments and on distributed pavement irregularities. Future research should extend the analysis to a wider set of riders and vehicle layouts, include quantitative road roughness descriptors, and investigate concentrated or impulsive irregularities, such as speed bumps, kerbs, and local obstacles. These conditions involve different excitation mechanisms and may pose additional comfort, controllability and safety challenges for compact micromobility vehicles.

Acknowledgements

Conceptualisation: A. D. Vella, A. Vigliani. Data curation: A. D. Vella. Formal analysis: A. D. Vella. Funding acquisition: A. Vigliani. Investigation: A. D. Vella. Methodology: A. D. Vella, A. Vigliani. Project administration: A. Vigliani. Resources: A. Vigliani. Software: A. D. Vella. Supervision: A. Vigliani. Validation: A. D. Vella. Visualisation: A. D. Vella. Writing – original draft: A. D. Vella. Writing – review & editing: A. Vigliani.

Author contributions

CRediT: **Angelo Domenico Vella:** Conceptualization, Data curation, Formal analysis, Investigation, Methodology, Software, Validation, Visualization, Writing – original draft, Writing – review & editing; **Alessandro Vigliani:** Funding acquisition, Investigation, Methodology, Project administration, Resources, Supervision, Writing – original draft, Writing – review & editing

Disclosure statement

No potential conflict of interest was reported by the author(s).

Data availability statement

Experimental data will be made available on reasonable request.

ORCID

Angelo Domenico Vella http://orcid.org/0000-0001-8253-0061
Alessandro Vigliani http://orcid.org/0000-0001-6423-9852

References

[1] Paddan GS, Griffin MJ. Evaluation of whole-body vibration in vehicles. J Sound Vib. 2002;253:195–213. doi:10.1006/jsvi.2001.4256
[2] He R, Sandu C, Khan AK, et al. Review of terramechanics models and their applicability to real-time applications. J Terramech. 2019;81:3–22.
[3] Little E, Handrickx P, Grote P, et al. Ride comfort analysis: practice and procedures, SAE Technical Paper 990053. 1999.
[4] Kumar KS, Pal S, Sethi RC. Objective evaluation of ride quality of road vehicles, SAE Technical paper. 1999.
[5] Demic M, Lukic J, Milic Ž. Some aspects of the investigation of random vibration influence on ride comfort. J Sound Vib. 2002;253:109–128. doi:10.1006/jsvi.2001.4252
[6] Múčka P, Stein GJ, Tobolka P. Whole-body vibration and vertical road profile displacement power spectral density. Veh Syst Dyn. 2020;58:630–656. doi:10.1080/00423114.2019.1595675
[7] Kat C-J, Skrickij V, Shyrokau B, et al. Vibration-induced discomfort in vehicles: a comparative evaluation approach for enhancing comfort and ride quality. SAE Int J Veh Dyn Stab. 2024;8(2):139–153. doi:10.4271/10-08-02-0009
[8] Mahmood A, Kat C-J, Els PS. Ride comfort optimization with handling constraints over rough terrain. J Terramech. 2026;122:101105. doi:10.1016/j.jterra.2025.101105
[9] Peng Y, Wu Z, Fan C, et al. Assessment of passenger long-term vibration discomfort: a field study in high-speed train environments. Ergonomics. 2022;65:659–671. doi:10.1080/00140139.2021.1980113
[10] Wu J, Qiu Y. Modelling and ride comfort analysis of a coupled track-train-seat-human model with lateral, vertical and roll vibrations. Veh Syst Dyn. 2022;60:2988–3023. doi:10.1080/00423114.2021.1933088

[11] Tiwari SK, Kumar R, Garg N. Noise and vibration in metro rail transit systems. Transp Res D Transp Environ. 2026;151:105124. doi:10.1016/j.trd.2025.105124
[12] Huang Y, Li J. Effects of vertical vibration on sitting comfort in civil aviation during the cruising flight. Ergonomics. 2023;66:524–535. doi:10.1080/00140139.2022.2098383
[13] Huang Y, Li J. Discomfort estimation for vertical whole-body vibration in the aircraft cabin considering the duration and static sitting comfort. Ergonomics. 2024;67:327–338. doi:10.1080/00140139.2023.2221420
[14] Li X, Huang Y, Ni K, et al. Integrated discomfort modelling of combined noise and vibration exposure in turbofan aircraft cabin. Ergonomics. 2025:1–14. doi:10.1080/00140139.2025.2592988
[15] Kim MS, Kim KW, Yoo WS. Method to objectively evaluate subjective ratings of ride comfort. Int J Automot Technol. 2011;12:831–837. doi:10.1007/s12239-011-0095-8
[16] Hiemstra-van Mastrigt S, Groenesteijn L, Vink P, et al. Predicting passenger seat comfort and discomfort on the basis of human, context and seat characteristics: a literature review. Ergonomics. 2017;60:889–911. doi:10.1080/00140139.2016.1233356
[17] Deubel C, Ernst S, Prokop G. Objective evaluation methods of vehicle ride comfort – a literature review. J Sound Vib. 2023;548:117515. doi:10.1016/j.jsv.2022.117515
[18] Eboli L, Mazzulla G, Pungillo G. Measuring bus comfort levels by using acceleration instantaneous values. Transp Res Proc. 2016;18:27–34. doi:10.1016/j.trpro.2016.12.004
[19] Maltinti F, Rassu N, Ventura R, et al. Driving style evaluation: novel comfort scales for urban buses. IEEE Trans Intell Transp Syst. 2025;26:15436–15452. doi:10.1109/TITS.2025.3604621
[20] Guastadisegni G, De Pinto S, Cancelli D, et al. Ride analysis tools for passenger cars: objective and subjective evaluation techniques and correlation processes – a review. Veh Syst Dyn. 2024;62:1876–1902. doi:10.1080/00423114.2023.2259024
[21] Papaioannou G, Shen C, Rothhämel M, et al. Occupants' comfort: what about human body dynamics in road and rail vehicles? Veh Syst Dyn. 2025;63:1241–1299. doi:10.1080/00423114.2025.2504113
[22] International Standard. Mechanical vibration and shock – evaluation of human exposure to whole-body vibration – part 1: general requirements, BS ISO 2631-1:1997, 1997.
[23] International Standard. Mechanical vibration – measurement and evaluation of human exposure to hand-transmitted vibration – part 1: general requirements, BS EN ISO 5349-1:2001, 2001.
[24] British Standards Institution. Guide to measurement and evaluation of human exposure to whole-body mechanical vibration and repeated shock, BS 6841:1987, 1987.
[25] Butler L, Yigitcanlar T, Paz A, et al. How can smart mobility bridge the first/last mile gap? Empirical evidence on public attitudes from Australia. J Transp Geogr. 2022;104:103452. doi:10.1016/j.jtrangeo.2022.103452
[26] Torabi K F, Araghi Y, van Oort N, et al. Passengers preferences for using emerging modes as first/last mile transport to and from a multimodal hub case study Delft Campus railway station. Case Stud Transp Policy. 2022;10:300–314. doi:10.1016/j.cstp.2021.12.011
[27] Ma Q, Xin Y, Yang H, et al. Connecting metros with shared electric scooters: comparisons with shared bikes and taxis. Transp Res D Transp Environ. 2022;109:103376. doi:10.1016/j.trd.2022.103376
[28] Badia H, Jenelius E. Shared e-scooter micromobility: review of use patterns, perceptions and environmental impacts. Transp Rev. 2023;43(5):811–837. doi:10.1080/01441647.2023.2171500
[29] Siebert FW, Ringhand M, Englert F, et al. Braking bad–Ergonomic design and implications for the safe use of shared E-scooters. Saf Sci. 2021;140:105294. doi:10.1016/j.ssci.2021.105294
[30] Zagorskas J, Burinskienė M. Challenges caused by increased use of e-powered personal mobility vehicles in European cities. Sustainability. 2019;12:273. doi:10.3390/su12010273
[31] Gössling S. Integrating e-scooters in urban transportation: problems, policies, and the prospect of system change. Transp Res D Transp Environ. 2020;79:102230. doi:10.1016/j.trd.2020.102230

[32] Bozzi AD, Aguilera A. Shared E-scooters: a review of uses, health and environmental impacts, and policy implications of a new micro-mobility service. Sustainability. 2021;13:8676. doi:10.3390/su13168676
[33] Şengül B, Mostofi H. Impacts of E-Micromobility on the sustainability of urban transportation – a systematic review. Appl Sci. 2021;11:5851. doi:10.3390/app11135851
[34] Abduljabbar RL, Liyanage S, Dia H. The role of micro-mobility in shaping sustainable cities: a systematic literature review. Transp Res D Transp Environ. 2021;92:102734. doi:10.1016/j.trd.2021.102734
[35] Cafiso S, Di Graziano A, Marchetta V, et al. Urban road pavements monitoring and assessment using bike and e-scooter as probe vehicles. Case Stud Const Mater. 2022;16:889. doi:10.1016/j.cscm.2022.e00889
[36] Kopplin CS, Brand BM, Reichenberger Y. Consumer acceptance of shared e-scooters for urban and short-distance mobility. Transp Res D Transp Environ. 2021;91:102680. doi:10.1016/j.trd.2020.102680
[37] Aarhaug J, Fearnley N, Johnsson E. E-scooters and public transport – complement or competition? Res Transp Econ. 2023;98:101279. doi:10.1016/j.retrec.2023.101279
[38] Dias G, Arsenio E, Ribeiro P. The role of shared E-Scooter systems in urban sustainability and resilience during the COVID-19 mobility restrictions. Sustainability. 2021;13:7084. doi:10.3390/su13137084
[39] Štefancová V, Kalašová A, Čulík K, et al. Research on the impact of COVID-19 on micromobility using statistical methods. Appl Sci. 2022;12:8128.
[40] Li D, Lasenby J. Investigating impacts of COVID-19 on urban mobility and emissions. Cities. 2023;135:104246.
[41] Gao J, Sha A, Huang Y, et al. Evaluating the cycling comfort on urban roads based on cyclists' perception of vibration. J Clean Prod. 2018;192:531–541. doi:10.1016/j.jclepro.2018.04.275
[42] Gao J, Sha A, Huang Y, et al. Cycling comfort on asphalt pavement: Influence of the pavement-tyre interface on vibration. J Clean Prod. 2019;223:323–341. doi:10.1016/j.jclepro.2019.03.153
[43] Chen H-C, Chen W-C, Liu Y-P, et al. Whole-body vibration exposure experienced by motorcycle riders – an evaluation according to ISO 2631-1 and ISO 2631-5 standards. Int J Ind Ergon. 2009;39:708–718. doi:10.1016/j.ergon.2009.05.002
[44] Paudel M, Fah Yap F. Front steering design guidelines formulation for e-scooters considering the influence of sitting and standing riders on self-stability and safety performance. Proc Inst Mech Eng Part D J Autom Eng. 2021;235:2551–2567. doi:10.1177/0954407021992176
[45] Agúndez AG, García-Vallejo D, Freire E. An electric kickscooter multibody model: equations of motion and linear stability analysis. Multibody Syst Dyn. 2024;62:493–524. doi:10.1007/s11044-024-09974-4
[46] Vella AD, Vigliani A. Research on the longitudinal dynamics of an electric scooter. SAE Int J Veh Dyn Stab NVH. 2022;7:35–51. doi:10.4271/10-07-01-0003
[47] Garman CMR, Como SG, Campbell IC, et al. Micro-mobility vehicle dynamics and rider kinematics during electric scooter riding, SAE Technical Paper, 2020. doi:10.4271/2020-01-0935.
[48] Brunner P, Löcken A, Denk F, et al. Analysis of experimental data on dynamics and behavior of e-scooter riders and applications to the impact of automated driving functions on urban road safety, in: 2020 IEEE Intelligent Vehicles Symposium (IV), IEEE, 2020. p. 219–225. doi:10.1109/IV47402.2020.9304835.
[49] Cano-Moreno JD, Islán ME, Blaya F, et al. E-scooter vibration impact on driver comfort and health. Journal of Vibration Engineering & Technologies. 2021;9:1023–1037. doi:10.1007/s42417-021-00280-3
[50] Cano-Moreno JD, Cabanellas Becerra JM, Arenas Reina JM, et al. Analysis of E-scooter vibrations from health perspective: A case study. Machines. 2023;11:761.
[51] Gulino M, Vichi G, Zonfrillo G, et al. Comfort assessment for electric kick scooter decks, in: IOP Conf. Ser. Mater. Sci. Eng., IOP Publishing, 2022: p. 012043.
[52] Boglietti S, Ghirardi A, Zanoni CT, et al. First experimental comparison between e-kick scooters and e-bike's vibrational dynamics. Transportation Research Procedia. 2022;62:743–751. doi:10.1016/j.trpro.2022.02.092

[53] Ventura R, Ghirardi A, Vetturi D, et al. Comparing the vibrational behavior of e-kick scooters and e-bikes: Evidence from Italy. International Journal of Transportation Science and Technology. 2024;16:68–86. doi:10.1016/j.ijtst.2023.10.010
[54] Asperti M, Vignati M, Braghin F. Modelling of the vertical dynamics of an electric kick scooter. IEEE Trans Intell Transp Syst. 2021;23:9266–9274. doi:10.1109/TITS.2021.3098438
[55] Asperti M, Vignati M, Braghin F. Modeling of the Vertical Dynamics of a Kick e-Scooter on Distributed Road Irregularity, in: Advances in Dynamics of Vehicles on Roads and Tracks II: Proceedings of the 27th Symposium of the International Association of Vehicle System Dynamics, IAVSD 2021, August 17–19, 2021, Saint Petersburg, Russia, Springer, 2022: pp. 1070–1080. doi:10.1007/978-3-031-07305-2_99.
[56] Arslan E, Uyulan Ç Analysis of an e-scooter and rider system dynamic response to curb traversing through physics-informed machine learning methods. Proc Inst Mech Eng Part D J Autom Eng. 2023;237(7):1555–1571. doi:10.1177/09544070221100111
[57] Vaca Michilena EX, Cano-Moreno JD. Multibody dynamic analysis of an E-scooter considering asymmetric tire stiffness, speed, and surface roughness. Machines. 2026;14:120.
[58] Asperti M, Antoniazzi A, Vignati M, et al. Experimental analysis of electric kick scooter vertical dynamics: the effect of speed, tyre inflation pressure, rider mass and road pavement on rider comfort and health safety. Veh Syst Dyn. 2026;64(8):1420–1445. doi:10.1080/00423114.2025.2483344
[59] Vella AD, Digo E, Gastaldi L, et al. Statistical analysis of the vibrations transmitted from an electric kick scooter to riders. Exp Tech. 2024;48:803–813. doi:10.1007/s40799-023-00693-7
[60] Schedlinski C, Link M. A survey of current inertia parameter identification methods. Mech Syst Signal Process. 2001;15:189–211.
[61] Cano-Moreno JD, Arenas Reina JM, Islán Marcos ME, et al. The vertical stiffness of e-scooter tires. Latin Am Appl Res. 2024;54:299–301.
[62] Cantisani G, Bruno S, D'Andrea A, et al. Methods for measuring and assessing irregularities of stone pavements – part II. Sustainability. 2023;15:3715.
[63] Zoccali P, Loprencipe G, Galoni A. Sampietrini stone pavements: distress analysis using pavement condition index method. Appl Sci. 2017;7:669.
[64] Mansfield ER, Conerly MD. Diagnostic value of residual and partial residual plots. Am Stat. 1987;41:107–116. doi:10.1080/00031305.1987.10475457
[65] Velleman PF, Welsch RE. Efficient computing of regression diagnostics. Am Stat. 1981;35:234–242. doi:10.1080/00031305.1981.10479362

Appendices

Appendix A. ISO 2631-1 and ISO 5349 signal filtering

For the foot-deck interface ($i = D$), the transfer function $H_{Dj}(p)$ associated with the ISO 2631-1 weighting operator $\mathcal{H}_{Dj}\{\cdot\}$ for WB vibrations in standing position is computed as:

$$H_{Dj}(p) = H_{h,j}(p)H_{l,j}(p)H_{t,j}(p)H_{s,j}(p) \tag{A1}$$

where p represents the variable of the Laplace transform. The high-pass and low-pass filter are computed as:

$$H_{h,j}(p) = \frac{1}{1 + \frac{\sqrt{2}\omega_{1,j}}{p} + \left(\frac{\omega_{1,j}}{p}\right)^2} \tag{A2}$$

$$H_{l,j}(p) = \frac{1}{1 + \frac{\sqrt{2}p}{\omega_{2,j}} + \left(\frac{p}{\omega_{2,j}}\right)^2} \tag{A3}$$

while the frequency weighting is computed as

$$H_{t,j}(p)H_{s,j}(p) = \frac{1+\frac{p}{\omega_{3,j}}}{1+\frac{p}{\omega_{4,j}Q_{4,j}}+\left(\frac{p}{\omega_{4,j}}\right)^2}\frac{1+\frac{p}{\omega_{5,j}Q_{5,j}}+\left(\frac{p}{\omega_{5,j}}\right)^2}{1+\frac{p}{\omega_{6,j}Q_{6,j}}+\left(\frac{p}{\omega_{6,j}}\right)^2}\left(\frac{\omega_{5,j}}{\omega_{6,j}}\right)^2 \tag{A4}$$

The parameters in Equations (A2)–(A4) are reported in Table A1 where $\omega_n = 2\pi f_n$ with $n = 1,\ldots,6$.

For the hand-steering interface ($i = S$), the transfer function $H_{Sj}(p)$ associated with the ISO 5349 weighting operator $\mathcal{H}_{Sj}\{\cdot\}$ for HT vibrations is computed as:

$$H_{Sj}(p) = H_{b,j}(p)H_{w,j}(p) \tag{A5}$$

where the band-pass filter is computed as:

$$H_{b,j}(p) = \frac{p^2\omega_8^2}{\left(p^2+\frac{\omega_7 p}{Q_7}+\omega_7^2\right)\left(p^2+\frac{\omega_8 p}{Q_7}+\omega_8^2\right)} \tag{A6}$$

while the frequency weighting is computed as:

$$H_{w,j}(p) = \frac{(p+\omega_9)2\pi f_{10}^2}{\left(p^2+\frac{\omega_{10}p}{Q_{10}}+\omega_{10}^2\right)f_9} \tag{A7}$$

The parameters in Equations (A6) and (A7) are reported in Table A3 where $\omega_n = 2\pi f_n$ with $n = 7,\ldots,10$.

Appendix B. Other results

Figures A1 and A2 compare the three vehicles in terms of discomfort index (DI_i) as a function of the testing velocity v on the bike path surface (S_3) evaluated at the foot-deck ($i = D$) and hand-steering interface ($i = S$).

Table A1. Parameters of the ISO 2631-1 filter for comfort assessment.

Axis	f_1 [Hz]	f_2 [Hz]	f_3 [Hz]	f_4 [Hz]	Q_4 [–]	f_5 [Hz]	Q_5 [–]	f_6 [Hz]	Q_6 [–]	$k_{D,j}$ [–]
x/y	0.4	100.0	2.0	2.0	0.63	∞	–	∞	–	1
z			12.5	12.5	0.63	2.37	0.91	3.35	0.91	

The discomfort bands from ISO 2631-1 are reported in Table A2. Since the ISO 2631-1 comfort bands partially overlap, the upper bound of each region is used here to define non-overlapping intervals.

Table A2. Discomfort regions for whole-body vibrations according to ISO 2631-1.

Perception	Lower bound [m/s^2]	Upper bound [m/s^2]
Not uncomfortable	0	0.315
A little uncomfortable	0.315	0.63
Fairly uncomfortable	0.63	1
Uncomfortable	1	1.6
Very uncomfortable	1.6	2.5
Extremely uncomfortable	2.5	∞

Table A3. Parameters of the ISO 5349 filter for comfort assessment.

Axis	f_7 [Hz]	Q_7 [–]	f_8 [Hz]	f_9 [Hz]	f_{10} [Hz]	Q_{10} [–]	$k_{S,j}$ [–]
$x/y/z$	6.31	0.71	1258.9	15.915	15.915	0.64	1

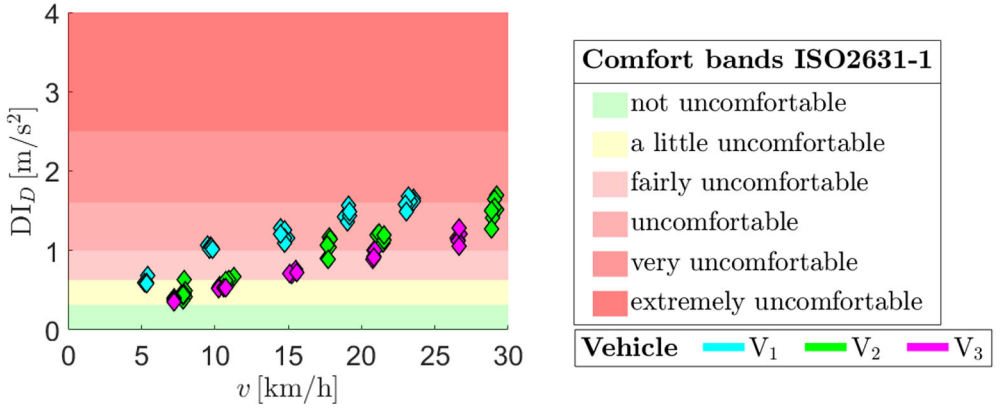

Figure A1. Discomfort index evaluated at the foot-deck interface for the three vehicles on the bike path for different vehicle velocities.

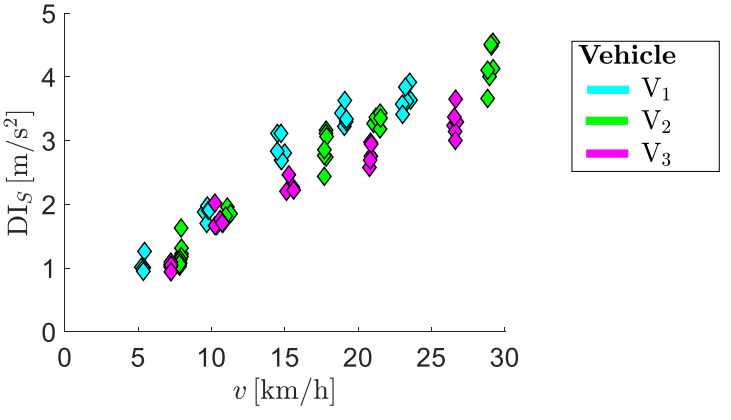

Figure A2. Discomfort index evaluated at the hand-steering interface for the three vehicles on the bike path for different vehicle velocities.

Table A4. Parameters used in the regression model.

Parameter	Operating condition	Value
q_R [–]	S_1	0
	S_2	1
	S_3	0.047
κ_0 [kN/mm]	V_1	0.1073
	V_2	0.0844
	V_3	0.0867

Appendix C. Regression model

The parameters related to road surface (q_R) and tyre stiffness (κ_0) included in the final regression model (Equation (9)) are reported in Table A4.

Table A5 reports WLS-estimated coefficients $\boldsymbol{\alpha}_i$ together with their standard errors (SE), the corresponding t-statistics (t-stat), and the associated two-sided p-values. For each coefficient, the test refers to the null hypothesis that the corresponding regression coefficient is equal to zero.

Table A5. WLS-estimated regression coefficients, standard errors, t-statistics and two-sided p-values for the foot-deck and hand-steering models.

	Human-vehicle interface							
	Foot-deck ($i = D$)				Hand-steering ($i = S$)			
Coefficient	Value	SE	t-stat	p-value	Value	SE	t-stat	p-value
$\alpha_{i,1}$ [m/s^2]	−1.16	0.109	−10.7	$\ll 10^{-3}$	−2.07	0.315	−6.50	$\ll 10^{-3}$
$\alpha_{i,2}$ [(m mm)/(s^2 kN)]	14.7	1.02	14.5		22.1	2.93	7.50	
$\alpha_{i,3}$ [m/s^2]	−2.84	0.164	−17.3		−4.58	0.473	−9.74	
$\alpha_{i,4}$ [(m mm)/(s^2 kN)]	33.3	1.97	16.8		95.1	5.68	16.9	
$\alpha_{i,5}$ [1/s]	0.14	0.007	20.2		0.474	0.02	23.50	
$\alpha_{i,6}$ [mm/(kN s)]	9.77	0.315	31.3		14.8	0.908	16.0	
$\alpha_{i,7}$ [1/m]	−0.063	0.003	−21.3		−0.088	0.009	−10.1	

Table A6. Correlation matrix of the retained non-constant regressors used in the WLS identification dataset.

	q_R	κ_0	$q_R\kappa_0$	v	$q_R\kappa_0 v$	$q_R v^2$
q_R	1	−0.07	0.99	−0.01	0.91	0.72
κ_0	−0.07	1	0.04	−0.27	−0.1	−0.23
$q_R\kappa_0$	0.99	0.04	1	−0.05	0.89	0.67
v	−0.01	−0.27	−0.05	1	0.27	0.47
$q_R\kappa_0 v$	0.91	−0.1	0.89	0.27	1	0.93
$q_R v^2$	0.72	−0.23	0.67	0.47	0.93	1

Table A7. Global significance indicators of the WLS regression model identified on V_1 and V_2 over S_1 and S_2.

	Global F	$df1$	$df2$	Global p-value
D	7124.7	6	178	$\ll 10^{-3}$
S	6432.7			$\ll 10^{-3}$

To document the correlation structure of the retained regressors, Table A6 reports the correlation matrix of the non-constant columns of the WLS design matrix used for the model identification.

The global significance indicators of the WLS regression models are reported in Table A7. The F-test compares the complete regression model with an intercept-only model. Here, $df1 = n_r$ is the number of regressors excluding the intercept, while $df2 = E - (n_r + 1)$ is the number of residual degrees of freedom.

Residual heteroscedasticity is assessed through the Breusch–Pagan test. The test is applied to the residuals of the final WLS models for the foot-deck and hand-steering interfaces, and the results are reported in Table A8. The null hypothesis corresponds to homoscedastic residuals.

Table A8. Breusch–Pagan test for residual heteroscedasticity in the WLS regression models.

	LM statistic	df	p-value
D	39.3	6	$\ll 10^{-3}$
S	48.8		$\ll 10^{-3}$